UNIVERSITY OF AMSTERDAM

MSc Physics

Advanced Matter and Energy Physics

Master Thesis

Förster resonance energy transfer from PbS quantum dots to silicon: The missing link towards singlet fission solar cells

by

Stefan Wil Tabernig

Stud.nr: 11404418

July 2018
60 ECTS
August 2017 - July 2018

1st Examiner:
Prof. Albert Polman

Supervisor:
Dr. Bruno Ehrler

2nd Examiner:
Prof. Femius Koenderink

AMOLF

Förster resonance energy transfer from PbS quantum dots to silicon: The missing link towards singlet fission solar cells,
August 2017 - July 2018

SUPERVISORS:
Prof. Albert Polman
Prof. Femius Koenderink
Dr. Bruno Ehrler

LOCATION:
Amsterdam

TIME FRAME:
August 2017 - July 2018

The only thing necessary for the triumph of evil is for good men to do nothing.

— Edmund Burke

ABSTRACT

One way to surpass the Shockley-Queisser limit is the use of a downconversion mechanism to obtain two excitons from an initial excitation by a high-energy photon. Singlet fission is such a downconversion process, enabling separation of a singlet-state exciton into two triplet-state excitons. Tetracene is a material that exhibits singlet fission and the energy of the triplet exciton (1.25 eV) lies above the bandgap of Si (1.12 eV). This means that if energy transfer from Tc to Si can be achieved, the high-energy range of the solar spectrum can be harvested much more efficiently by adding a Tc-layer on top of a Si solar cell. One way to achieve this energy transfer is by introducing PbS QDs as an intermediate. This geometry makes use of efficiently working Dexter energy transfer between Tc and PbS QDs. However, the mechanism for the subsequent transfer step from the PbS QDs to Si has not yet been identified. Here, we investigate Förster resonance energy transfer as a possible mechanism and use its theoretical framework to obtain a Förster model for our geometry. Furthermore, we compare this model with experiment by investigating the dependence of the QD PL-lifetime on the QD-Si separation. The results show that energy transfer with an efficiency of up to 15.3 % is possible. However, the data does not allow to draw a final conclusion regarding the underlying transfer mechanism.

PUBLICATIONS

Some ideas and figures have appeared previously in the following publication:

Stefan Wil Tabernig, Benjamin Daiber, Tianyi Wang, Bruno Ehrler; **Enhancing silicon solar cells with singlet fission: the case for Förster resonant energy transfer using a quantum dot intermediate**, *J. of Photonics for Energy, 8(2), 022008 (2018)*,
https://doi.org/10.1117/1.JPE.8.022008

ACKNOWLEDGEMENTS

I would like to express my sincere gratitude to the following individuals: First of all Benjamin Daiber for being a fantastic daily supervisor. Thanks for always making time when I needed to bother you with whatever question I had. Then, Bruno Ehrler for giving me the opportunity to do my internship in the Hybrid Solar Cells group and subsequently being an awesome supervisor, always providing useful feedback and showing the right direction throughout the project. Christian Dieleman for sharing his expertise on QDs and TianYi Wang for always pointing out interesting literature to me. Henk-Jan Boluijt for the design of the encapsulations. The rest of the HSC group for the nice atmosphere here at AMOLF and support in the lab. Furthermore, everyone at AMOLF who helped me throughout my project. My two examiners, Albert Polman and Femius Koenderink, for the grading of my thesis and presentation. The people who operate sci-hub for their commendable service to society. My friends, of course. And, last but not least, my parents for supporting me.

CONTENTS

1 INTRODUCTION 1
- 1.1 Working principle of a solar cell 1
  - 1.1.1 Charge carrier generation 1
  - 1.1.2 Charge carrier separation 2
- 1.2 Beyond ordinary solar cell structures 2
  - 1.2.1 The Shockley-Queisser limit 3
  - 1.2.2 Downconversion 3
- 1.3 Energy transfer mechanisms 4
- 1.4 Towards Tc - PbS QD - Si energy transfer 5
  - 1.4.1 Energy transfer from Tc to Si 5
  - 1.4.2 Energy transfer from Tc via PbS QDs to Si 6
- 1.5 Lead sulfide quantum dots (PbS QDs) 8

2 THEORY 11
- 2.1 Förster resonance energy transfer (FRET) 11
  - 2.1.1 FRET formalism 11
  - 2.1.2 The Förster distance R_0 12
  - 2.1.3 The overlap integral J 12
  - 2.1.4 FRET parameters for our geometry 12
- 2.2 Generalization of FRET to 2D- and 3D-acceptors 15
- 2.3 FRET from 1.2 eV PbS QDs to Si 18
  - 2.3.1 Predictions for R_0 and the point-model 18
  - 2.3.2 Plane and bulk model predictions 19
- 2.4 Future work 22

3 EXPERIMENTAL METHODS 23
- 3.1 Preparing the donor QDs 23
  - 3.1.1 PbS QD synthesis 23
  - 3.1.2 Surface passivation 24
  - 3.1.3 QD absorption and PL spectra 25
- 3.2 Engineering the donor-acceptor separation 26
  - 3.2.1 Sample preparation 26
  - 3.2.2 Deposition of SiO_2 on Si 27
  - 3.2.3 Determination of SiO_2 layer thickness 27
- 3.3 PbS QD deposition on Si/SiO_2 33
  - 3.3.1 Spincoating 33
- 3.4 TCSPC setup 33
  - 3.4.1 Focusing 35
  - 3.4.2 Encapsulation 35
- 3.5 Data collection and processing 37
  - 3.5.1 Data collection 37
  - 3.5.2 Data processing 38
- 3.6 Determination of the optimal measurement conditions 38
  - 3.6.1 TCSPC: possible sources for errors 39

3.6.2 QD-Si sample degradation 40
4 RESULTS & DISCUSSION 45
4.1 First indications of quenching of the QD PL 45
4.2 PL lifetime as a function of donor-acceptor separation 45
4.3 FRET efficiency 46
4.4 Discussion 46
4.4.1 Comparison with other models 50
4.4.2 Future work 50
5 SUMMARY 53

BIBLIOGRAPHY 55

ACRONYMS

FRET Förster resonance energy transfer

HOMO Highest occupied molecular orbital

LDOS Local density of optical states

LUMO Lowest unoccupied molecular orbital

PL Photoluminescence

QD Quantum dot

QY Quantum yield

RTA Rapid thermal annealing

SEM Scanning electron microscopy

SPAD Single photon avalanche diode

TCSPC Time correlated single photon counting

XPS X-ray photoelectron spectroscopy

1 INTRODUCTION

Following the Kyoto Protocol[1] and the Doha Amendment[2], the ratification of the Paris Agreement[3] by as many as 170 countries, which are responsible for 87.90% of global emissions, was the first big political step towards tackling climate change in 2015. While it is reassuring that most countries endorse climate friendly policies, they strongly rely on industry and research to develop solutions and initiate changes. One change required in order to come close to the optimistic goal of heating up earth by only 1.5 °C is the transition of the energy sector towards renewable energy sources. A large part of this is conversion of solar energy into heat and into the highest valued form of energy, electricity, via solar cells. The solar cell industry has grown exponentially over the past 50 years and the prices of solar cells have dropped accordingly, a correlation which is described by Swanson's law[4], in a similar style as Moore's law for transistors[5,6]. While this sounds encouraging, there is still a lot of research to be done on photovoltaic concepts, apart from ordinary silicon solar cells. Before we look into such promising innovative approaches, we briefly summarize the working principle of a conventional solar cell.

1.1 Working principle of a solar cell

1.1.1 Charge carrier generation

The basic idea behind a solar cell is the conversion of light into electrical energy. This means that an electric current has to be created from photons. The mechanism for this conversion process is the excitation of an electron into a higher energy state by a photon. In the case of a semiconductor, this corresponds to the excitation of an electron from the valence band into the conduction band. A similar mechanism exists for organic molecules, where such excitation occurs from the highest occupied molecular orbital (HOMO) into the lowest unoccupied molecular orbital (LUMO). The required energy to excite an electron from the lower lying state depends on the energy difference between conduction and valence band and is commonly referred to as bandgap energy or just bandgap. Photons with less energy than the bandgap cannot stimulate this process and are regarded as "lost" photons for the photovoltaic energy conversion. In the case of an excitation of an electron into the conduction band, a vacancy is left behind, which is called (electron-) hole. This hole represents a missing electron and is regarded as a positive charge carrier that complements

the electron. Together they initially form a hot electron-hole pair with a chemical energy corresponding to the excitation energy of the photon. This hot electron that has been excited will relax back towards the lowest available energy level of the conduction band, while the hot hole will move to the highest state in the valence band. The energy difference between the initial excitation state and this band edge state is dissipated via phonons, a process which is commonly referred to as thermalization.

1.1.2 Charge carrier separation

After photoexcitation, the electron could recombine with the hole by emission of a photon with an energy that corresponds to the band gap. For efficient solar energy conversion, the rate at which this event happens has to be slower than the charge extraction rate. Charge extraction requires that the electron and hole are separated from each other, for example via a p-n junction.
Such a junction consists of a semiconductor with an n-doped (excess of electrons) and a p-doped (excess of holes) region. At their interface there is a so-called depletion region, which extends into both components. The term "depletion" is used because this region is depleted from mobile charge carriers, as they diffuse across the p-n interface and recombine with their counterparts. However, immobile charge carriers, namely ionized atoms, are still present close to the interface, positively charged in the n-doped part, and vice versa in the p-doped part. This difference in charge causes an electric field that acts across the interface, in the opposite direction of the carrier diffusion. The system will assume a steady state, with a built-in voltage across the junction.
By contacting the two ends of the junction with, for example, two ohmic contacts and connecting them to an electrical load, one can use the built-in voltage to send the electrons from the p-doped end through the load towards the n-doped end, where they can recombine. Without continuous charge carrier generation by light, electrons and holes will travel past the load and recombine with their counterparts so that the built-in voltage vanishes over time. However, under constant illumination this carrier migration along the electric circuit can continue to power a load, providing electrical energy generated from light.

1.2 Beyond ordinary solar cell structures

The working principle described above is the fundamental framework for a working solar cell. Nowadays, solar cells can be made from ordinary semiconductors[7,8], more exotic compounds[8–10], multiple layers (tandem solar cells)[8,11,12] or nano-materials, like nanowires[13,14] and

quantum dots[15,16]. Still, owing to the facts that Si solar cells are cheap and that Si-based solar cell technologies are well established, it is hard to imagine a future in which Si solar cells will not play a significant role in energy production. So, instead of competing with Si solar cells, it is also worth investigating approaches that aim on improving present Si solar cell efficiencies. However, Si solar cell efficiencies are already close to the so-called Shockley-Queisser limit, which means that novel approaches to circumvent that limit need to be considered.

1.2.1 The Shockley-Queisser limit

The Shockley-Queisser limit (SQ limit)[11,17] describes the maximum theoretical efficiency for a single junction solar cell under standard test conditions. This gives an upper limit for the photo-conversion efficiency of 33.7 %[17]. Shockley and Queisser consider the following three major detrimental effects.
The first one is the fact that the solar cell - as any other body at non-zero temperature - exhibits thermal radiation. This means that some of the energy that is absorbed by the solar cell will be radiated away.
Secondly, the energy-hole pair generation is limited by the irradiation. According to the concept of detailed balance[11,17], the reverse mechanism must also be possible. This leads to the assumption that all recombination is radiative.
The third large contribution to the loss is the fact that only parts of the received electromagnetic spectrum can be used for charge carrier generation, as the energy of the incoming photons has to be above the bandgap of the absorbing material. Additionally, in the case of high energy photons that can excite carriers beyond the bandgap, the extra energy is lost as the charge carriers will relax towards the band edge. This energy loss mechanism is referred to as "quantum defect", stemming from the fact that one photon can only generate one pair of charge carriers, no matter how high its energy might be.

1.2.2 Downconversion

By nature, scientists tend to regard the word "limit" as something worth challenging. This becomes obvious when looking at the variety of approaches proposed to surpass the SQ-limit.
One subset of those approaches is spectral management. This includes creation of one high energy photon from two low energy photons via photon upconversion[18,19], as well as downconversion[20,21], which refers to the inverse process. Downconversion architectures make use of the excess energy of the incoming light, which would otherwise be lost as heat. Singlet fission[22–24] is such a mechanism, although it does not create two low-energy photons from a high-energy photon, but instead two low-energy excitons from one high-energy ex-

citon. The initial creation of an exciton can be caused by light, and excitons can be dissociated into electron-hole pairs, which corresponds to the in- and output of a solar cell.
Singlet fission is a process where an excited singlet-state exciton separates into two triplet-state excitons with roughly half the singlet energy. The term singlet-state denotes a system with a spin quantum number of 0, while the term triplet-state corresponds to a spin quantum number of 1. Usually, transitions from one of these states to the other are forbidden, as this would require spin-mixing. However, two triplet-state excitons can form a system with an overall spin quantum number of 0, which means that if the energies are right, transitions between a singlet exciton and such a triplet exciton pair can happen[22,23], thus allowing for singlet fission.
In principle, these excitons can be dissociated[25–27] to obtain separated electrons and holes, which could contribute to an electric current, like in a solar cell[23]. As the excitons cannot dissociate into electrons and holes in the singlet fission material itself, one has to transfer them into an environment with a higher dielectric constant[27] or use a heterojunction[26] to enable exciton dissociation. In our case we use tetracene (Tc) as the singlet fission material and silicon (Si) as the acceptor for the excitons. Another way to harvest the energy of the triplets would be by only transferring the triplet exciton energy into silicon, which means that the excited triplet has to relax back into the singlet ground state. This will be the approach we will investigate throughout this thesis.

1.3 Energy transfer mechanisms

Figure 1 shows the four most significant energy transfer mechanisms for a donor-acceptor junction. The first one shown is charge transfer, which involves separation of the exciton into electron and hole and subsequent extraction of the two carriers at different ends (Figure 1a). Another possible mechanism is Dexter energy transfer (DET)[28]. Dexter transfer works by exchanging an excited electron from the donor (D) for a ground state electron of the acceptor (A) (Figure 1b). This means that in principle the whole exciton has been transfered. For this to happen, the condition of having proper wavefunction overlap has to be met, which requires the D-A separation to be less than 1 nm. Radiative energy transfer is the relaxation of the donor into the ground state by emission of a photon. The photon is absorbed by the acceptor, which completes the energy transfer process (Figure 1c). As long as the D-A separation is far smaller than the lateral dimension of the acceptor, this process can be regarded as independent of D-A separation.
FRET is the near-field component of a generalized photon mediated energy transfer mechanism of which radiative energy transfer is the

far-field component[29]. The process basically follows the same steps, with the difference being that a virtual photon mediates the dipole-dipole interaction (Figure 1d). The main consequence of this, making FRET so interesting[30], is that FRET shows a distance dependence that follows an inverse sixth power law. In most systems[31–33], this allows for systems with D-A separations of up to 10 nm to exhibit highly efficient FRET, outcompeting any other transfer mechanism.

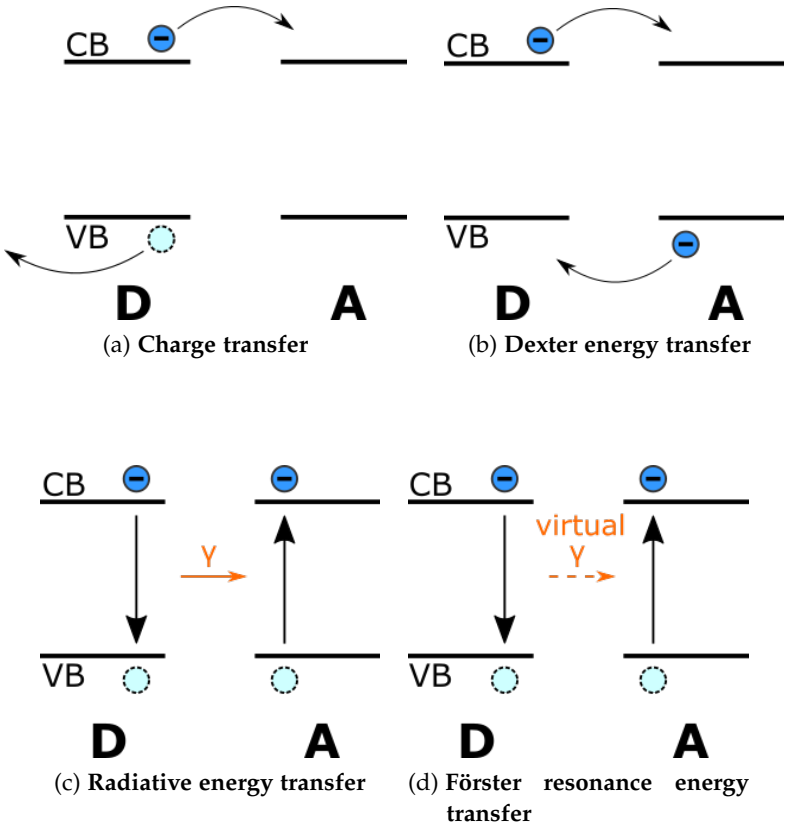

(a) **Charge transfer** (b) **Dexter energy transfer** (c) **Radiative energy transfer** (d) **Förster resonance energy transfer**

Figure 1: **Possible energy transfer mechanisms**
The upper row schematically shows electron-mediated energy transfer mechanisms, while the bottom row shows photon-mediated energy transfer mechanisms. The schemes show how an excited donor (PbS QD) interacts with an acceptor in the ground state.

1.4 Towards Tc - PbS QD - Si energy transfer

1.4.1 Energy transfer from Tc to Si

The basic geometry we investigate is a Tc-Si geometry (Figure 2). However, transferring the energy of the triplet excitons from Tc into Si is limited to electron-mediated transfer mechanisms. The reason for that is that the transition of a triplet-state exciton into the (singlet)

ground state is spin-forbidden, which causes long triplet lifetimes[34]. In spite of this constraint, energy transfer mechanisms that are electron mediated could be an option, however such a transfer has not been shown to work yet.

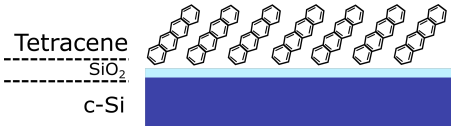

Figure 2: **Tc - Si geometry**
The base architecture of a singlet fission enhanced Si solar cell: A Tc-layer on top of SiO_2 of the underlying crystalline Si, which is part of the solar cell.

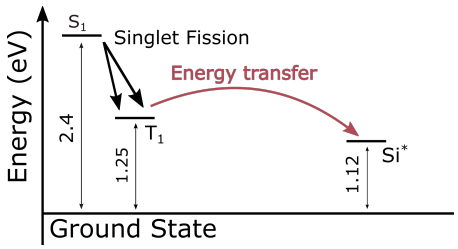

Figure 3: **Tc - Si Jablonski diagram**
The Jablonski diagram illustrates how the energy levels of Tc compare to Si. Singlet fission turns the 2.4 eV singlet-state exciton S_1 into two 1.25 eV triplet-state excitons T_1. The following energy transfer step towards Si is the mechanism in question. Note that the transfer from the T_1 state to Si is downhill in energy ($\Delta E \approx 130meV$).

The transfer mechanism we will investigate, is the introduction of an intermediate layer which serves as acceptor for the Tc-generated triplet excitons and as donor of energy towards Si. Here, we attempt to use lead sulfide (PbS) quantum dots (QDs) as such a layer, with the aim of circumventing Tc-Si energy transfer issues by introducing a radiative state to enable photon-mediated transfer mechanisms.

1.4.2 Energy transfer from Tc via PbS QDs to Si

Figure 4 and Figure 5 illustrate how such an architecture could look like physically and energetically. Note that while Figure 4 shows a mono-layer coverage of QDs on Si, this does not necessarily need to be the the case (see Subsection 2.1.4). The SiO_2-layer in between the QDs is in principle an unwanted spacer as it increases the QD - Si separation, which in general lowers the energy transfer efficiency, but will play an important role during our experiments in Chapter 3.
Figure 5 shows the new energy landscape after the introduction of PbS QDs compared to Figure 3. It shows that for the energy transfer steps to be energetically downhill, the QDs need a bandgap of 1.25 eV

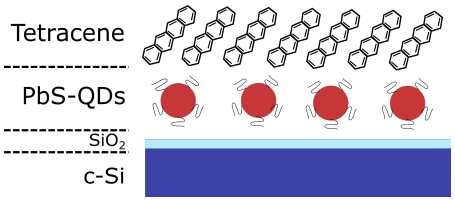

Figure 4: **Intended Tc - PbS QD - Si geometry**
The geometry shown places Tc on PbS QDs and Si, which is covered by a SiO_2 layer.

or lower, while the emission has to be at or above 1.12 eV. These constraints arise from the T_1 energy as upper boundary and the bandgap of Si as lower boundary. The choice of the QD bandgap is confined even more strongly, because the Stokes shift causes the emission of the QDs to be at lower energy than their absorption. The Stokes shift for PbS QDs is around 120 meV[35], which means that the QD bandgap has to be close to the T_1 energy to make sure that the QD PL is above the Si bandgap.

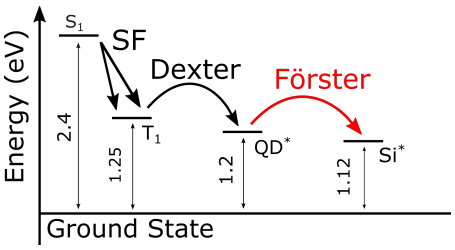

Figure 5: **Jablonski diagram for the intended geometry**
The two energy steps are indicated and labeled as "Dexter" and "Förster". The first step has been shown to work via Dexter energy transfer[36,37], while the mechanism for the second step remains to be determined, but we suspect Förster resonance energy transfer to be dominant.

1.4.2.1 Tc - PbS QD energy transfer

The first step in the proposed geometry requires transfer of excitons from Tc towards the PbS QDs (Figure 6). This has been shown to work by two groups independently[36,37], with efficiencies close to unity.

1.4.2.2 PbS QD - Si energy transfer

The big advantage of using the quantum dots as an intermediate transfer stage is that the excitons in the QDs are bright states, which is possible because of strong spin-orbit coupling in the QD[38] introduced by the Pb atoms. This property allows for spin-mixing which means that the spin state of the exciton is not relevant anymore when it comes to radiative relaxation to the ground state. With this, energy transfer mechanisms that rely on radiative states become an option.

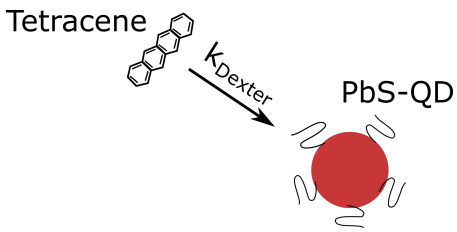

Figure 6: **Dexter energy transfer from Tc to PbS QDs**
Energy transfer in a Tc - PbS QD system happens via Dexter energy transfer.

While we will focus on the case for Förster resonance energy transfer (FRET) for our system, we will briefly mention and explain if other possible processes could apply to our geometry.

Charge transfer would require a hole acceptor layer on top of the Tc or PbS QD layer, which would introduce undesirable absorption losses. DET will probably contribute to the overall energy transfer, but should be outcompeted by photon-mediated energy transfer mechanisms. While radiation of photons towards the Si substrate might be an efficient path to follow, Förster resonance energy transfer (FRET) has the capability to outcompete it. FRET also acts at a distance that is larger than the characteristic transfer distance for DET and would be easy to achieve by ordinary deposition methods. In Chapter 2 we will take a closer look at FRET, the associated formalism as well as its application to our geometry.

1.5 Lead sulfide quantum dots (PbS QDs)

We will use (colloidal) quantum dots (QDs) in our device geometry. QDs are semiconductor nanoparticles[39] of a few nanometers to a few tens of nanometers in size. They are usually stabilized by ligands, which are molecules of sizes up to 1.5 nm.
Their small size induces strong confinement of charge carriers in the crystals, changing the optical[40,41] and electronic properties[41] of the material. Near the bandgap, the confinement causes discretization of the energy states of the material. This means that, optically, they behave similarly to atoms, strongly absorbing specific wavelengths of the electromagnetic spectrum, while weakly absorbing the rest. The wavelength region where the QDs absorb the strongest is referred to as first absorption peak (see Figure 14). For smaller wavelengths the QDs take on a continuously increasing absorption, indicating that the QDs recover the bulk properties of the semiconductor. By tuning the confinement, one can adjust the position of the first absorption peak (also referred to as bandgap) of the quantum dots. The confinement can be tuned by changing the size of the QDs, which is determined by the synthesis parameters (see Subsection 3.1.1). Equation 1 shows the

empirically determined relation between size (d) and bandgap (E_0) for PbS QDs[40].

$$E_0(d) = 0.41 + \frac{1}{0.0252\ d^2 + 0.283\ d} \tag{1}$$

2 THEORY

2.1 Förster resonance energy transfer (FRET)

FRET is a non-radiative dipole-dipole interaction, which requires a donor and acceptor to participate. In his paper on "Intermolecular energy migration and fluorescence"[29] , Förster introduced a formalism to describe the rate at which a donor transfers energy to an acceptor, from which we can determine the FRET efficiency. In the following, we will introduce this formalism and extend it in such a way that it fits our geometry, assuming a QD emission centered around 1.2 eV.
In the course of the theoretical treatment of our system a lot of attention will be paid to the dependence of the efficiency of the system on the molar absorption coefficient of the acceptor material. The reason for that is that Si has an indirect bandgap[42]. This means that the given system is fundamentally different from well studied FRET systems, such as QD-QD[32] and molecular[31] systems. Furthermore, this implies that there is a realistic possibility that the given system is not capable of utilizing FRET for energy transfer. This will be explored in Subsection 2.1.4.

2.1.1 FRET formalism

The FRET efficiency $\eta_{FRET}$is given by Equation 2, where the the FRET rate k_{FRET} is compared to the sum over all decay rates that affect the donor. Assuming that all the other rates are not affected by the presence of an acceptor, one can summarize them as a constant base rate of the donor in absence of an acceptor $k_{D,0}$. This base rate can be related to the donor lifetime in absence of an acceptor via $k_{D,0} = \frac{1}{\tau_{D,0}}$

$$\eta_{FRET} = \frac{k_{FRET}}{\sum_i k_i} = \frac{k_{FRET}}{k_{FRET} + k_{D,0}} \tag{2}$$

The FRET rate describes how fast two fluorophores[31,33], which are approximated to be point dipoles, exchange energy with each other. It turns out that k_{FRET} strongly depends on the D-A separation r_{DA}, following an inverse sixth power law (Equation 3). Apart from that, the rate is a function of $k_{D,0}$ as well as the so-called Förster distance R_0.

$$k_{FRET} = k_{D,0} \left(\frac{R_0}{r_{DA}} \right)^6 \tag{3}$$

2.1.2 The Förster distance R_0

The parameter R_0 is a system specific constant, which is often used to determine if efficient FRET can occur for a given system. It is defined as that distance between donor and acceptor at which the FRET rate equals 50 % of the total rate. As Equation 4 shows, apart from constants, R_0 depends on the donor quantum yield (Q_D), an orientation parameter (κ^2), the refractive index of the separating medium (n) and J, which is the so-called overlap integral.

$$R_0^6 = \frac{9000 \ln(10)}{128 \pi^5 N_A} \cdot \frac{Q_D \kappa^2 J}{n^4} \tag{4}$$

...with N_A representing the Avogadro constant.

The orientation parameter κ^2 can in principle assume any value between 0 and 4, depending on the relative orientation of the donor and acceptor transition dipoles towards each other. n is the refractive index of the separating medium. It depends on the material between donor and acceptor. The quantum yield Q_D describes the ratio of emitted photons to incoming photons.

2.1.3 The overlap integral J

The (spectral) overlap integral (J) indicates how well the donor emission and the acceptor absorption align spectrally. It is defined by Equation 5, with $\overline{f_D}$ being the normalized donor emission, $\alpha_{M,A}$ the molar absorption coefficient of the acceptor and λ the wavelength.

$$J = \int_0^\infty \overline{f_D} \alpha_{M,A} \lambda^4 d\lambda \tag{5}$$

2.1.4 FRET parameters for our geometry

The QDs exhibit rotational symmetry, which means that the dipole orientation will be isotropic. This leads to an overall randomized relative orientation of the transition dipoles, which yields $\kappa^2 = \frac{2}{3}$[43].
The value n has to be chosen by taking into account that our separating medium is not completely homogeneous. Here we will follow Yeltik et. al.[44] by imagining a straight line that connects the QD and the Si substrate. We then simplify the separating medium by assuming that the SiO_2-layer is the only contribution along that line, which leads to a refractive index of $n_{SiO_2} = 1.45$.
However, one has to keep in mind that the interacting component is the exciton in the QD and as such our imagined line that connects the exciton and the substrate would also pass through parts of the

QD itself. This means that the refractive index of the PbS QD and especially of the ligands would need to be added and a weighted average would need to be calculated. In general, this would lead to an increase of the effective refractive index, as the refractive index of PbS is far higher than that of SiO_2. Organic ligands like oleic acid (1.45[45]) and 3-mercatopropyonic acid (1.5[46]) show similar refractive indices as SiO_2 and inorganic ligands like ZnI_2 are so small that their contribution can be neglected.
While one could in principle easily account for the contributions to the refractive index by QDs and ligands, the ligands pose a problem as there is space in between the ligands with a refractive index different of that of the ligand. In fact, there is a lot of empty space in between the ligands which has to be accounted for to find the overall refractive index[47]. As this is not trivial, we choose the approximation mentioned in the beginning, where the SiO_2-layer is assumed to be the only contribution to the separating medium. This approximation can be assumed to hold true as long as SiO_2 is the dominating material across most of the separation range. Note that this is not the case for smaller separations at the order of the size of the QDs and less.
Q_D is a parameter that can vary strongly, depending on QD size[40], ligands[48], excitation wavelength[49], present QD concentration (density)[49] and on whether the QDs are dissolved or in solid state[50]. For an average QD size of 3.4 nm, which corresponds to 1.2 eV[40], the range of Q_D can be found to range from up to 55 %[49] in dissolved form and up to 15 %[50] after deposition.
The QD coverage influences our system in different ways. One of them is that the QDs can transfer energy amongst each other at small separations. With every transfer step, there is a certain probability of finding a trap, which means that a higher QD density will come with a bigger loss of energy. This loss is represented by a reduced quantum yield Q_D.
Denser coverages also lead to stronger parasitic absorption, meaning that the QDs will absorb photons that were meant to pass through the Tc layer and be absorbed by Si.
On the other hand, a low coverage means that triplet excitons from the Tc-layer are less likely to find a QD to transfer to, as there are less QDs within the diffusion length of the exciton.
We treat these effects by assuming sub-monolayer coverage of the QDs on Si. Such a coverage would ideally minimize the interaction between quantum dots while still providing a QD-QD separation that is smaller than the diffusion length of triplet excitons in Tc. The Förster distance for QD-QD systems is around 8 nm[32,51], which means that a separation of twice this distance should be sufficient to suppress Förster transfer between QDs. The triplet exciton diffusion length determines how close the QDs should be to each other to make sure that every exciton from the Tc layer can find a QD and is around

400 nm[52,53]. Thus, the range of QD-QD separations we can use for our system ranges from around 20 to 400 nm. Of course, to increase the chance of a triplet exciton finding a QD, denser coverages are favorable, and thus we will go on and assume a QD-QD separation of 50 nm.
Such a coverage means that one QD with a radius of 1.7 nm (corresponding to a bandgap of 1.2 eV) occupies an area of 50 nm x 50 nm. By dividing the volume of the QD, which we assumed to have a spherical shape, by the area occupied by one QD, we obtain an effective QD layer thickness of $d_{QD,eff} = 9 * 10^{-3} nm$. Using this, we can write down a function for the light intensity as function of distance traveled through our effective QD medium, using the Beer-Lambert law (Equation 6).

$$I_{QD}(\lambda) = I_0(\lambda) \cdot e^{-\alpha_{QD}(\lambda) d_{QD,eff}} \tag{6}$$

...where $I_{QD}(\lambda)$ denotes the intensity after passing through the QD layer, $I_0(\lambda)$ the incident intensity (AM1.5 solar spectrum[54]) and $\alpha_{QD}(\lambda)$ the absorption coefficient of 1.2 eV PbS QDs[55]. From this we can calculate the integrated relative intensity loss ΔI_{rel}, which is given by Equation 7, where the Tc singlet excitation wavelength (λ_{Tc}) and the Si bandgap (λ_{Si}) serve as the integration boundaries.

$$\Delta I_{rel} = \frac{\int_{\lambda_{Tc}}^{\lambda_{Si}} (I_0(\lambda) - I_{QD}(\lambda)) d\lambda}{\int_{\lambda_{Tc}}^{\lambda_{Si}} I_0(\lambda) d\lambda} \tag{7}$$

...which provides us with an integrated relative intensity loss of $\Delta I_{rel} = 0.0001\%$. This confirms our assumption that the parasitic QD absorption for our assumed coverage is negligible.
$\alpha_{M,A}$ is especially interesting for our system, as the molar absorption coefficient of Si is weak close to the band gap, due to Si having an indirect bandgap (see Figure 7). This will lead to smaller values for J compared to other systems[31–33], which could in principle lead to the conclusion that FRET is not possible for our system according to the theory. Section 2.2 will answer this question.
Figure 7 visualizes this indirect bandgap penalty for our system. If the slope of $\alpha_{M,A}$ were steeper around 1.2 eV, the area enclosed by $\alpha_{M,A}$ and the QD PL would be larger, corresponding to a higher value for J. It also becomes clear that slight changes in the emission energy of the QDs have a strong impact on the enclosed area, due to the exponential shape of $\alpha_{M,A}$. According to Yeltik et.al.[44], FRET is phonon-assisted, which means that the energy transfer might work more efficiently at room temperature than our calculations in Section 2.2 predict.

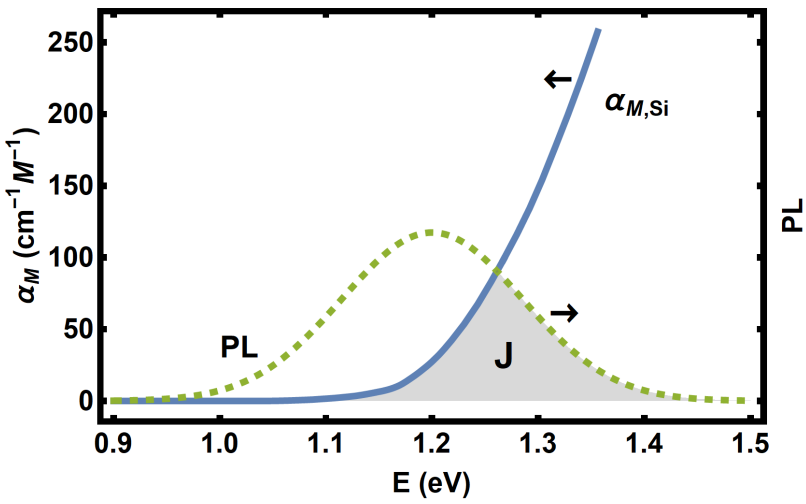

Figure 7: **Visualization of** J
The figure shows the normalized QD PL as a green, dashed line and $\alpha_{M,Si}$ as a blue line. The full width at half maximum (FWHM) of the PL was taken to be 200 meV, which agrees well with literature[47]. The shaded area corresponds to the overlap integral J.

2.2 Generalization of FRET to 2D- and 3D-acceptors

The formalism described above is accurate for the description of point donor and point acceptor systems. However, our system involves a bulk acceptor, which requires us to introduce some modifications to the formalism in order to obtain a valid description. We will extend the given point-point model to a point-plane model and subsequently to a point-bulk model. Physically, the last model is probably the one that is the closest to reality, but for the sake of completeness we will also include the point-plane model, as it has previously been used to describe layered system of QDs of different size[56].

The modifications we need to make affect the formula for k_{FRET}, which describes point-point interaction. By integration over the x-y plane we obtain a new FRET rate which describes energy transfer from a donor towards a plane with the dipole distributed across it (Equation 8).

$$\begin{aligned} k_{FRET} &= \frac{R_0^6}{\tau_{D,0}} \int\int_{0,0}^{\infty,2\pi} \frac{r}{(R_{DA}(r_{DA}, r))^6} dr d\phi \\ &= \frac{R_0^6}{\tau_{D,0}} \int\int_{0,0}^{\infty,2\pi} \frac{r}{\left(\sqrt{r_{DA}^2 + r^2}\right)^6} dr d\phi \\ &= \frac{R_0^6}{\tau_{D,0}} \cdot \frac{\pi}{2r_{DA}^4} \end{aligned} \tag{8}$$

...where $R_{DA}(r_{DA}, r)$ is the distance between the donor dipole and an infinitesimally small acceptor dipole somewhere on the plane. After integration over the Si surface (r, ϕ represent polar coordinates) one obtains the FRET rate as function of distance from the surface, with r_{DA} now representing the distance component that is perpendicular to the plane. Figure 8b shows the used parameterizations for the integration steps made in this section.

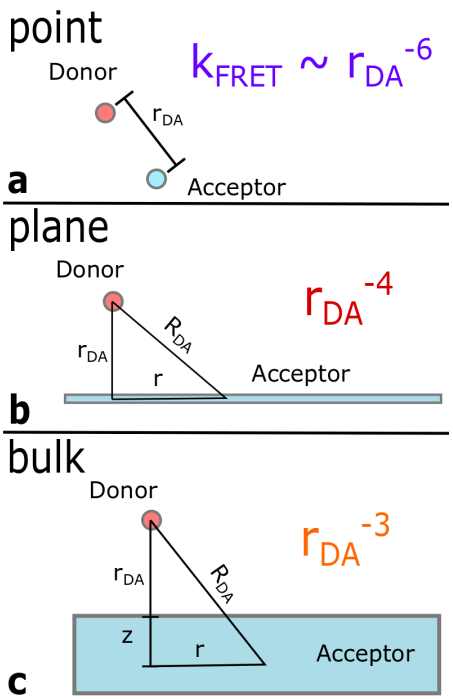

Figure 8: **Schematic representation of all three geometries**
We see three images which correspond to the point (a), plane (b) and bulk (c) model. The parameterizations for every model are indicated as well as their corresponding distance dependence.

The plane model assumes a dipole distribution across the acceptor surface, but in reality, they are distributed throughout the bulk, which means that we have to perform another integration step to finalize our formula.

Additionally, we now have to take into account that we will change the effective separating medium, as transfer towards a point inside the silicon means that parts of the intermediate medium is Si itself. To take this into account, we first need to introduce a total refractive index (n_{tot}), which will replace the current refractive index of the separating medium. For that, let us again think of a line that directly connects the point donor and a point somewhere in the acceptor. Let $z' = z + r_{DA}$ be the full length of this line and z the length of the part of the line that extends into the acceptor. Lastly, let r_{DA} represent the length of the part of the line that passes through the SiO_2-layer (see Figure 8). Now we can determine the total refractive index by

weighing the two individual refractive indices with their corresponding lengths on our imagined line (Equation 9).

$$n_{tot}(r_{DA} + z) = n_{SiO_2} \cdot r_{DA} + n_{Si} \cdot z \tag{9}$$

...with the refractive index of Si (n_{Si}) taken to be 3.55, which is its value at 1.2 eV[57]. After rearranging we obtain Equation 10:

$$\begin{aligned} n_{tot} &= \frac{n_{SiO_2} \cdot r_{DA} + n_{Si} \cdot z}{(r_{DA} + z)} \\ &= n_{SiO_2} \cdot \frac{r_{DA} + \frac{n_{Si}}{n_{SiO_2}} \cdot z}{(r_{DA} + z)} \end{aligned} \tag{10}$$

This expression can be plugged into Equation 4, leading to a slightly changed expression for the Förster distance (R_0'):

$$\begin{aligned} (R_0')^6 &= \frac{9000 \ln(10)}{128 \pi^5 N_A} \cdot \frac{Q_D \kappa^2 J}{n_{tot}^4} \\ &= \frac{9000 \ln(10)}{128 \pi^5 N_A} \cdot \frac{Q_D \kappa^2 J}{n_{SiO_2}^4} \cdot \left(\frac{r_{DA} + \frac{n_{Si}}{n_{SiO_2}} \cdot z}{(r_{DA} + z)} \right)^{-4} \\ &= R_0^6 \cdot \left(\frac{r_{DA} + z}{r_{DA} + \frac{n_{Si}}{n_{SiO_2}} \cdot z} \right)^4 \end{aligned} \tag{11}$$

Having obtained a new expression for R_0, we can now introduce R_0' into Equation 8 and integrate over z:

$$\begin{aligned} k_{FRET} &= \frac{\pi}{2} \int_0^\infty \frac{(R_0')^6}{(r_{DA} + z)^4} dz \\ &= \frac{\pi}{2} R_0^6 \int_0^\infty \frac{1}{(r_{DA} + z)^4} \left(\frac{r_{DA} + z}{r_{DA} + \frac{n_{Si}}{n_{SiO_2}} \cdot z} \right)^4 dz \\ &= \frac{\pi}{2} R_0^6 \int_0^\infty \frac{1}{\left(r_{DA} + \frac{n_{Si}}{n_{SiO_2}} \cdot z \right)^4} dz \\ &= \frac{\pi}{2} R_0^6 \frac{n_{SiO_2}}{n_{Si}} \int_0^\infty \frac{1}{u^4} du \\ &= -\frac{\pi}{6} R_0^6 \frac{n_{SiO_2}}{n_{Si}} \left(0 - \frac{1}{r_{DA}^3} \right) \\ &= \frac{\pi}{6} R_0^6 \frac{n_{SiO_2}}{n_{Si}} \frac{1}{r_{DA}^3} \end{aligned} \tag{12}$$

...with a substitution of variables where $u = r_{DA} + \frac{n_{Si}}{n_{SiO_2}} z$ and $du = \frac{n_{Si}}{n_{SiO_2}} dz$.

Interestingly, the prefactor turns out to be independent of distance, which might seem counterintuitive because we just introduced a distance dependence for the total refractive index. From a mathematical point of view, this distance dependence is lost due to our choices for the integration limits and the only relict which we can find in our final formula is the $\frac{n_{SiO_2}}{n_{Si}}$ factor. We can also define a new effective Förster distance $R_{0,eff}$ for the bulk model, by incorporating the prefactors so that we obtain Equation 13. $R_{0,eff}$ is the distance at which half of the total population decays by FRET. This value is different from the value for the point model because the integration over three dimensions weakened the distance dependence, which yields higher efficiencies for larger separations, as can be seen in the following section.

$$R_{0,eff} = \left(\frac{\pi}{6}\frac{n_{SiO_2}}{n_{Si}}\right)^{\frac{1}{6}} R_0 \tag{13}$$

2.3 FRET from 1.2 eV PbS QDs to Si

2.3.1 Predictions for R_0 and the point-model

The most relevant parameter for our system is R_0 as it gives an indication of the relevant distance range can be. Figure 9 shows the Förster distance for different Q_D as a function of QD emission. There is a steep decrease of R_0 for emission below the Si bandgap of 1.12 eV. This can be attributed to the exponential decrease of the molar absorption coefficient of Si below the bandgap. Above the bandgap of Si, the change as function of emission energy is weaker. Shaded in gray is the relevant energy range for the QDs, with the Tc T_1 states as upper limit and the Si bandgap as lower limit. Depending on the QD emission energy and on the QDs' quantum yield, R_0 can range from 0.8 nm to 1.5 nm. This range of values is encouraging as it implies that FRET transfer can be efficient at physically realistic distances. However, this is much smaller than R_0 in molecular[31,33] or QD-QD systems[32].

We can now use R_0 in order to calculate FRET rates and efficiencies. The FRET rate requires knowledge about the base rate ($k_{D,0}$), but for the FRET efficiency (η_{FRET}), $k_{D,0}$ cancels out during the calculations and thus makes η_{FRET} independent of $k_{D,0}$. Figure 10 shows the predictions that the initial point model provides, given R_0 from Figure 9. We again compare for different QYs and compare efficiencies for two different separations. For 1 nm separation, high efficiencies can be reached even for low QYs, with an efficiency of 65 % possible for a QY of 20 %, and close to unity efficiency for an optimistic QY of 100 %. In contrast, doubling the distance to 2 nm massively reduces the efficiencies that can be expected. Even the most optimistic case

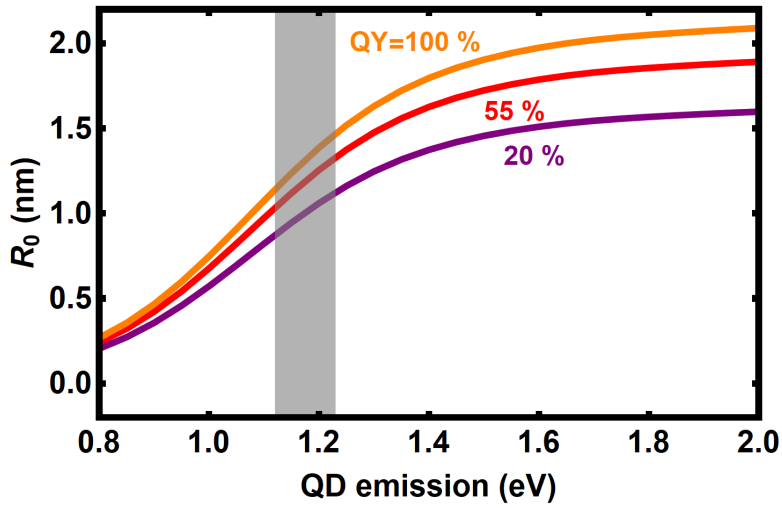

Figure 9: R_0 **as a function of QD emission**
The colors denote different QYs, and the same correspondence will be used for Figure 10 and Figure 11. The relevant energy range for the QDs is indicated by the shading

would yield less than 20 % transfer efficiency. This fact underlines how important it is to make sure that the QDs are close to the Si substrate.

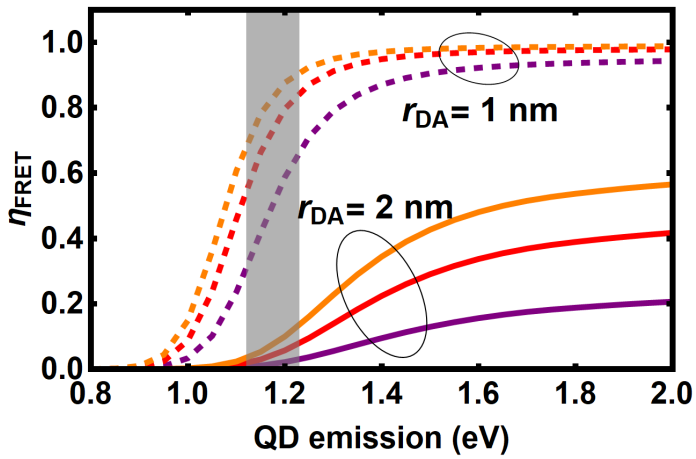

Figure 10: **FRET efficiency for the point-model**
The dashed lines correspond to 1 nm separation and the others to 2 nm separation. The colors indicate different QY, as specified in Figure 9.

2.3.2 Plane and bulk model predictions

The upper panel of Figure 11 shows how the consideration of a planar acceptor affects the predictions by the model. While the predicted

efficiencies for both distances increase, the stronger change can be observed for 2 nm separation. While still not being high, the efficiencies now range from 10 % to almost 50 %, depending on the QY. If we consider a bulk acceptor (bottom panel Figure 11), we observe a slightly different picture. The bulk model yields worse efficiencies than the plane model for both distances. Compared to the point model, the efficiencies for 1 nm are also worse, whereas for 2 nm the efficiencies are slightly increased.

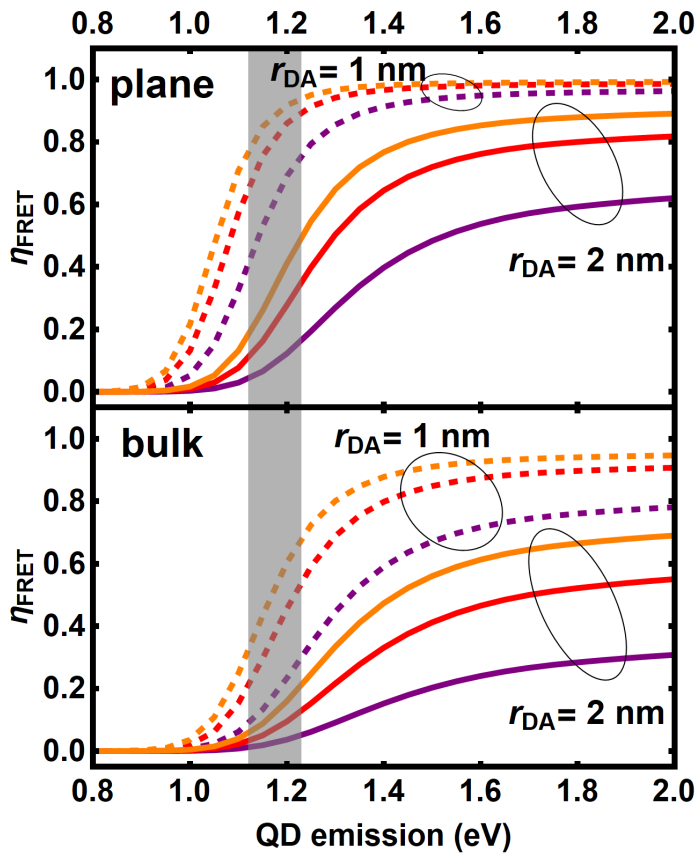

Figure 11: **FRET efficiencies for the plane and bulk model**
The dashed lines correspond to 1 nm separation and the solid lines to 2 nm separation. The colors indicate different QY, as specified in Figure 9.

The improvement of efficiencies from the point to the plane model is what one would expect, considering that the QD donor has more infinitesimal acceptors available as transfer partners. However, the same consideration should be valid for the step from the plane model to the bulk model, but this is not the case.
Figure 12 compares the predicted efficiencies of the three models as a function of D-A separation. There, it becomes clear that the different distance dependence is the origin of the counter-intuitive result ob-

tained above. The plane model yields the highest efficiencies across most of the distance range (0.8 nm-4.7 nm). It is difficult to see in Figure 12, but the point model yields the highest efficiencies up to 0.8 nm and is then surpassed by the plane model. The bulk model starts off as the weakest, surpassing the point model slightly below 2 nm and seems to approach the plane model for larger separations. What is not clearly visible in this figure is that the bulk model actually surpasses the plane model around 4.7 nm.
On a side note, the intersections between the individual model curves are the same for any chosen value of R_0, which means that in the case of larger Förster distances, the bulk-model would appear as the one with the highest yields. This counterintuitive behavior arises because the difference between the models at short distances becomes marginal for large R_0 and with increasing D-A separation, the bulk-model FRET efficiency decreases the slowest.
But why is the bulk model weaker than any of the other models in general? The reason for that is that for small separations like we have them here, the dipoles in the bulk are on average further away from the donor than it is the case for the point or plane model. This means that as long as the donor is so close that the average distance of the infinitesimal acceptor points in the bulk matters, the bulk model will yield lower efficiencies.

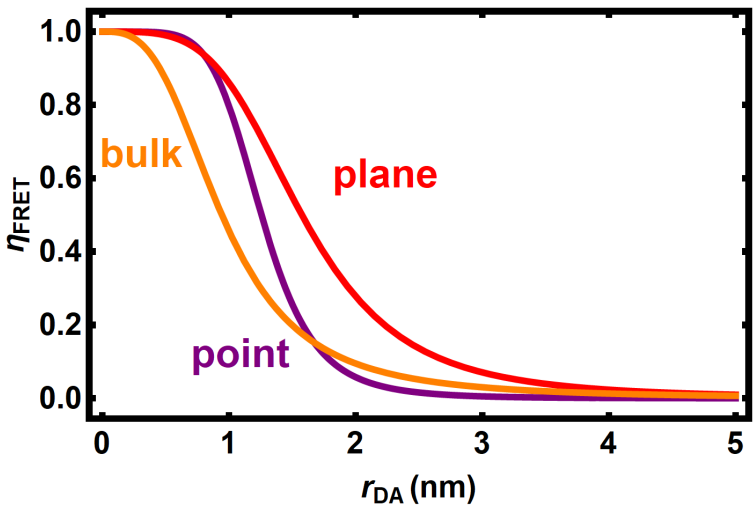

Figure 12: **FRET efficiencies as function of D-A separation**
The three models are compared to each other and their intersection denote the region where one of them starts predicting higher efficiencies than the other.

2.4 Future work

For Further improvement of the theoretical consideration of our system, the description of the point donor dipole has to be extended towards an extended dipole. Such a description is usually not needed as long as the dipole size is much smaller than the relevant distances, but in our case this is not true anymore. The size of the QD exciton is 1.8 nm, and thus in the same order as the relevant transfer distances. This means that the near-field cannot be accurately described by a mere r_{DA}^{-3} dependence. In order to take the extended dipole into account one has to follow the derivation of Förster without making the point-dipole approximation. Instead of a single r_{DA} dependent term, this would yield a formula for k_{FRET} that consists of a sum of r_{DA} dependent terms of higher orders, as well as more than one orientation parameter (κ_i^2).

Another, probably minor improvement would be to describe the refractive index of the SiO_2-layer more accurately. While we think that our approximation of SiO_2 as the sole separating material is justifiable, the refractive index of SiO_2 could be described in more detail. First of all, this would mean that the wavelength dependence of its refractive index should be taken into account. In principle this could be done but would require the inclusion of n in the overlap integral. This would change the definition of R_0 and J. As the refractive index of SiO_2 is approximately constant across the range we are interested in, we did not attempt to redefine R_0 and J here.
According to literature[58], the refractive index of SiO_2 grown on Si is also thickness dependent. It is reported that close to the interface n_{SiO_2}, goes up to 2.8 from an initial 1.45, due to changes in composition. However, a mathematical representation of this change of n_{SiO_2} could not be found in literature, which is why we neglected it.

Unlike Si, materials such as GaAs, InP, and CdTe exhibit a direct bandgap. Studying FRET for such systems would be interesting as it allows to investigate the full potential of geometries that are similar to the QD-Si system.

3 EXPERIMENTAL METHODS

The predictions obtained from the model in Section 2 need to be checked experimentally, to find out about the accuracy of the model as well as the physical feasibility of FRET in the QD-Si system. This is done by measuring the PL lifetime of the PbS QDs as a function of distance from a Si substrate. As the lifetime is the inverse of the PL decay rate, a change in the lifetime can be an indication for a contribution by the FRET rate.
We will work with the following geometry: A 1.5 eV PbS QD (donor) layer on top of a Si (acceptor) substrate. The Si substrate has an oxide (SiO2) layer, which acts as our donor acceptor separation. By changing the thickness of this oxide layer we can create samples with varying D-A separations. To determine the energy transfer efficiency from the QDs to Si we will look at the time resolved photoluminescence (tr-PL) of the QDs, as function of distance. When the separation decreases, the PL lifetime is expected to decrease, because the donor and acceptor interact more strongly with each other and thus the radiative rate competes with a faster energy transfer rate. We obtain a curve for the total decay rate (inverse of PL lifetime) of the PbS QDs as a function of donor-acceptor separation. Assuming that all other rates ($k_{D,0}$) stay constant, the change of the total rate $k_{D,0} + k_{FRET}$ as a function of distance then corresponds to a change of the FRET rate $k_{FRET}(r_{DA})$.
Figure 13 shows our observable and how it relates to $k_{FRET}(r_{DA})$. Significant changes in the measured rate will only occur for separations below 4 nm, according to this curve. The procedure for obtaining the data points corresponding to Figure 13 is as follows: After a sample has been prepared with the desired SiO_2 thickness, QDs are spin coated onto it. The last step is measuring the time resolved PL via the time correlated single photon counting (TCSPC) setup.

3.1 Preparing the donor QDs

3.1.1 PbS QD synthesis

The colloidal QDs used in this work were synthesized by Ruirt Bosma, a previous Master student, via the hot injection method[59]. In order to obtain the 1.5 eV QDs we measured, the following recipe was used[60]: Most chemicals were purchased from Sigma-Aldrich. For those that were not, the distributor will be indicated.
The octadecene was degassed by heating it to 80 °C under vacuum. A

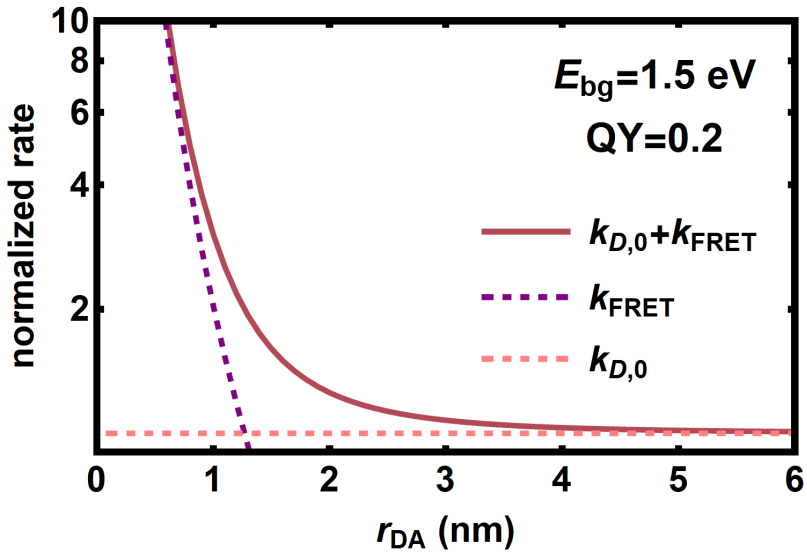

Figure 13: **The observable $k_{D0} + k_{FRET}$ normalized by k_{D0}**
The figure shows how the observable total rate is the sum of the constant base rate in absence of an acceptor $k_{D,0}$ and the distance dependent FRET rate k_{FRET}.

20 ml syringe was filled with 0.213 ml of bis(trimethylsilyl)sulphide (synthesis grade) together with 10 ml of octadecene (technical grade 90 %) in a glove box (<0.5 ppm H2O, <0.5 ppm O2) environment. 0.45 g of PbO (99.999 %, Alpha Aesar), 1.34 g of oleic acid (technical grade 90 %) and 14.2 g of octadecene are mixed together in a three-necked Schlenk flask. At a temperature of 95 °C and under vacuum this formed a clear solution. Then, the temperature increased to around 170 °C in a nitrogen environment. Now, the Schlenk flask containing the lead precursor is transferred to a heating mantle at room temperature. As soon as the temperature has reached the injection temperature of 100 °C (for 1.5 eV QDs), the sulphur precursor is injected into the flask with the solution being vigorously stirred. Right after the injection, 20 mL of anhydrous hexane (T =6 °C) is added to quench the reaction.

3.1.2 Surface passivation

For I_2 surface passivation, we follow Lan et. al.[61]. After the synthesis, the QDs are precipitated with acetone in a glovebox. After centrifuging for 4-10 mins at 4000-5000 rpm the liquid is disposed of, followed by vacuum-drying of the precipitate overnight. The quantum dots are then re-dispersed in toluene (>99.9 %) to obtain a concentration of 150 mg ml^{-1}. Now a 25 mM iodine (99.999 %) in toluene solution is added to the QD solution at a 1:5 ratio and stirred for 24 h. Afterwards the QDs are precipitated with methanol and centrifuged at

1500-5000 rpm for 2-5 min. The residual fluid was disposed of and after a night of vacuum-drying the QDs were dispersed in octane to obtain a 37.5 mg ml^{-1} solution. Eventually, this solution was diluted with octane to obtain a 5 mg ml^{-1} solution, which was used in the lifetime measurements, if not stated otherwise.

3.1.3 QD absorption and PL spectra

To measure absorption spectrum of QDs, the QD solution was first diluted and then filled into a cuvette. Figure 14 shows the absorption spectra for QDs with different bandgaps. The first exciton peaks are clearly visible in all four cases and the peak broadening is comparable to values reported in literature[47]. The measurements were conducted using a LAMBDA 750 UV-vis spectrometer from PerkinElmer.

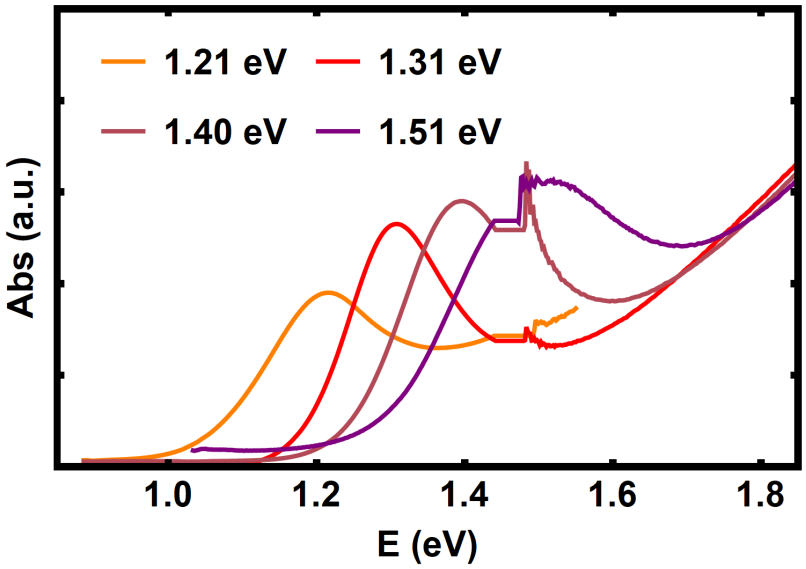

Figure 14: **QD absorption spectra**
Absorption spectra of 5 mg ml^{-1} QD solutions around the first exciton peak for varying QD sizes. The plateau between 1.4 and 1.5eV is due to a malfunction of a detector in the UV-vis setup and not of physical origin.

PL spectra were measured (see Figure 15) only for 1.2 eV and 1.5 eV QDs, as those are the ones that are most relevant for the intended geometry and the ones used for the experimental part, respectively. The detector (Ocean Optics USB4000) is Si based and can only be used to measure PL down to 1.19 eV. While the Stokes shift we observe for the 1.5 eV QDs agrees well with literature values, the observed anti-Stokes shift for the 1.2 eV QDs does not. In general, one would expect a Stokes shift around 120 meV for such a QD size. The explanation for this observation is probably that the QDs have degraded. Most probably, the solution somehow got into contact with oxygen and

subsequently the QDs oxidized. This process is known to induce a blue shift in the QD PL[62], which is what we observe.

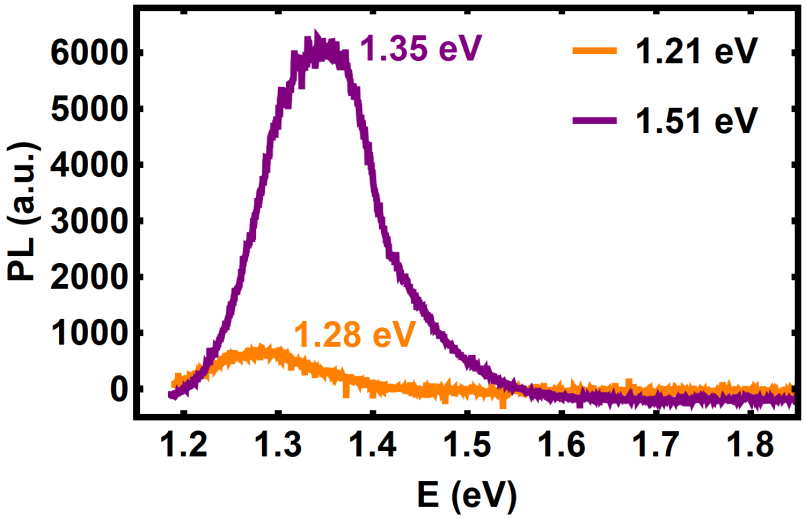

Figure 15: **QD PL spectra**
The PL as a function of energy is compared between 1.2 eV and 1.5 eV QDs. The 1.5 eV QDs show a Stokes shift of 160 meV, while the 1.2 eV QDs show a anti-Stokes shift of 70 meV.

3.2 Engineering the donor-acceptor separation

The donor-acceptor separation is adjusted by changing the thickness of the SiO_2 layer on the Si substrate. SiO_2 layer thicknesses between 2.3 and 70.0 nm were deposited via rapid thermal annealing (RTA). As there is always a native SiO_2 layer of approximately 1.9 nm on the substrate, the native oxide had to be removed and regrown in a controlled manner (stable ambient conditions) to get substrates with SiO_2 layer thicknesses below the native oxide layer thickness. The thicknesses were subsequently measured via ellipsometry and X-ray photoelectron spectroscopy (XPS).

3.2.1 Sample preparation

Si substrates of a size of (10 x 10) mm² are cleaned by hand using a toothbrush dipped in a soap-water solution for around 30 s and subsequently rinsed with DI-water. Then, they are sonicated for 20 min subsequently in water, aceton, and isopropanol. Afterwards, the samples are taken out of the isopropanol and dried with a N_2 gun and brought into a N_2 glovebox environment (O_2 < 0.1 ppm, H_2 < 0.1 ppm) for storage or directly undergo SiO2 layer growth or removal.

3.2.2 Deposition of SiO_2 on Si

The growth of SiO_2 on the Si substrates was done via RTA. The RTA device is basically an oven with a Si-wafer on a fragile quartz framework acting as a sample holder in the middle. The samples were inserted into the oven and in a first step heated to the desired temperature under a constant N_2-flow of 1 $l\,min^{-1}$ for 60 s. The growth started with step 2, in which the N_2-flow is cut off and replaced by O_2 at a certain flow rate (see Table 1). After that, the chamber is cooled down for 60 s under N_2-flow of 1 $l\,min^{-1}$. The growth conditions were chosen according to curves from literature[63] and then growth recipes were formed and labeled according to the initially intended thickness (Table 1).

Table 1: **Growth parameters for SiO_2 growth on top of the native oxide layer**
d... prospective thickness (according to literature[63])
t... growth time
r... O_2-flow rate
T... growth temperature

d / nm	t / s	r / $l\,min^{-1}$	T / °C
2	10	1.5	775
4	90	1.5	775
6	20	1.0	1100
8	40	1.0	1100
12	90	1.0	1100
20	150	1.0	1100
60	900	1.0	1100

3.2.3 Determination of SiO_2 layer thickness

For an accurate determination of the SiO_2 layer thickness, ellipsometry in combination with XPS was used. The use of both techniques was necessary to be able to cover the full thickness range relevant for the experiments. Ellipsometry loses sensitivity for thicknesses less than 7 nm[64] due to the fact that it is a bulk measurement and requires a minimum thickness to be accurate. On the contrary, thickness measurements via XPS are limited to the escape depth of the photoelectrons and thus is only accurate up to maximum 15 nm, depending on the measured material[64]. This leaves a window where both techniques can be used, in order to check that the two independent measurements were consistent with each other. Both techniques are described in the following.

3.2.3.1 Ellipsometry

In ellipsometry, not the thickness, but the real and imaginary parts of the refractive index of the sample are measured. We use a VB-400 ellipsometer from J.A. Woollam. The user has to provide a model, which describes the different layers on the substrate, to the program. The program then fits the measured n and k values to the literature values and determines what layer thickness leads to the best fit. In this case, a simple model, consisting of only the Si substrate and the SiO_2 layer on top, was used. For Si, the material file "Si.mat" was used, but for SiO_2, there were two possibilities. The "SiO2_jaw.mat" file contains literature data for thermally grown oxide, while the "ntve_jaw.mat" file contains reference values for native oxide. Due to the fact that the substrates always have a thin native oxide layer (grown right after HF-etching), on which additional oxide was thermally grown, it is not straightforward to choose a file for the fitting. The native oxide fitting gives smaller errors for small thicknesses close to the actual native oxide thickness, while the thermal oxide fitting becomes more accurate for thicker oxide layers. This opens up two possibilities: The first one would be to perform both fits and use the thickness value with the smaller error, as the error stems from the fitting accuracy. A second option would be to weigh the two results according to their mean square error, which is provided with every fit. A comparison of the two individual fits and their weighed average, which we chose to regard as the actual thickness, can be found in Figure 16.

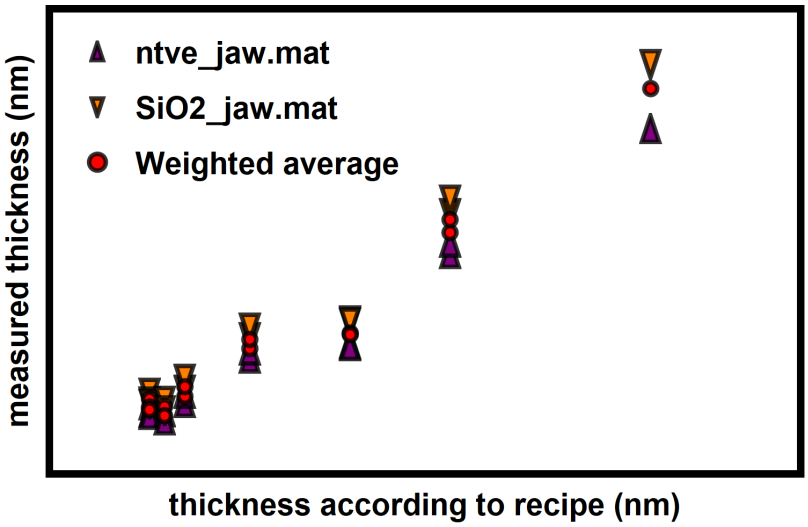

Figure 16: **Comparison of ellipsometry fitting methods**
Thicknesses according to the two fitting methods and their weighted average are shown. The native oxide fitting seems to underestimate thicknesses above 8 nm.

3.2.3.2 X-ray photoelectron spectroscopy

The values obtained in the ellipsometry measurements below 7 nm seem to be consistent with the trend and the expected thickness, but to be sure in that regime, XPS has to be employed. Thickness measurement via XPS works by comparing two characteristic peaks, the Si-elemental and Si-oxygen peaks. Figure 17 shows the characteristic peaks of the XPS spectra of Si with different SiO_2 thicknesses. Depending on what Si is bound to, several peaks and side peaks can be found between 99 and 104 eV[65], two of which correspond to Si bound to either Si or O (see Figure 18). Following[64,66], the ratio between the areas under those two peaks can be used to determine the SiO_2 thickness, as the areas are proportional to the amount of bonds. In order to obtain the thickness, Equation 14 has to be used, which relies on a couple of parameters[65,66] that will be explained in the following.

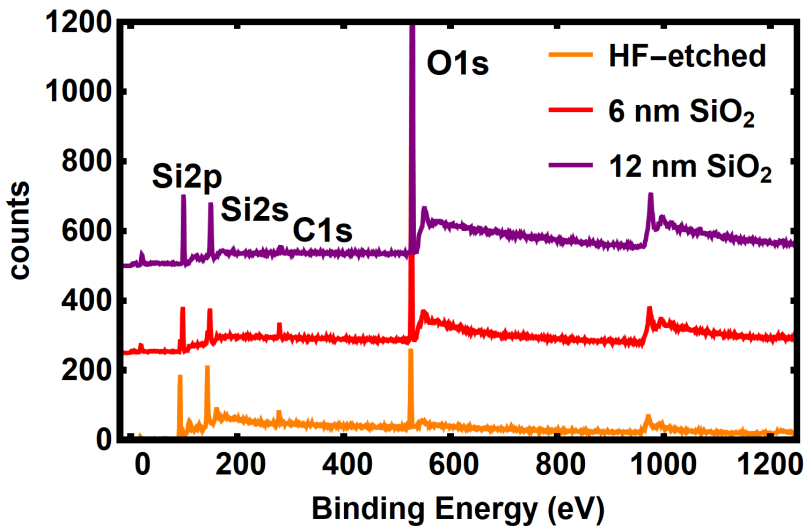

Figure 17: **Full range XPS spectra of Si samples**
XPS spectra of Si samples with different SiO_2 thickness. The C1s-peak is commonly used as a reference peak[67] for the comparison of different XPS-spectra. The decay behavior of the counts towards higher binding energies following pronounced peaks is a loss feature. The "HF-etched" label corresponds to a sample that has been exposed to air for 3 h after HF-etching and prior to the measurement.

$$d_{oxy} = \lambda_{oxy} \cdot \sin(\alpha) \cdot \mathrm{Ln}\left(\frac{I_{oxy}}{\beta \cdot I_{Si}} + 1\right) \tag{14}$$

...where...

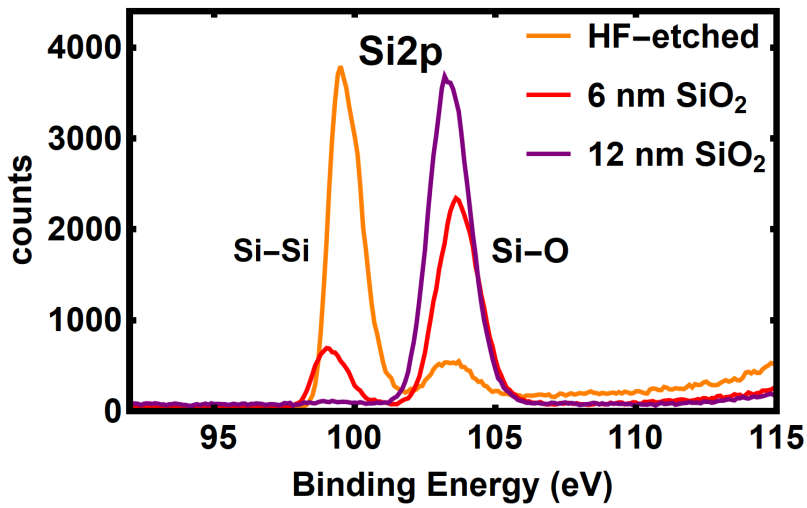

Figure 18: **XPS spectra around the Si2p-peaks**
Note that this is a separate measurement for this specific energy range and not a close-up of Figure 17, hence the higher number of counts and improved energy resolution. The Si-elemental and Si-oxygen peaks are located at 99.4 eV and 103.5 eV, respectively.

d_{oxy}	SiO_2-thickness
λ_{oxy}	photoelectron escape depth in SiO_2
	$(\lambda_{oxy} = (2.96 \pm 0.19)nm$
α	take off angle (Here: 90°)
I_i	area under corresponding peak

...and...

$$\beta = \frac{Y_{oxy} D_{oxy} \lambda_{oxy}}{Y_{Si} D_{Si} \lambda_{Si}} \tag{15}$$

...where...

Y_i	photoelectron yield
	$(Y_{oxy} = 0.69, Y_{Si} = 0.59)$
D_i	number of Si atoms per unit volume
	$(D_{oxy} = 2.28 * 10^{22}, D_{Si} = 5.00 * 10^{22})$
λ_{Si}	photoelectron escape depth in Si
	$(\lambda_{Si} = (2.11 \pm 0.13)nm)$

Two methods to determine the peak area were investigated and compared (Figure 19). Both methods initially fit Gaussians to the two

peaks, but they differ in the choice of integration limits and integrate over different functions. The first one, labeled "slope method" sets the integrations limits to the point where the first derivative of the fitted function reaches a threshold value close to zero. The second method, "sigma method" sets the integration limits to a multiple of the peak broadening. We find that both methods lead to the same thickness, however, the "slope method" fits the asymmetry of the Si-Si peak[68] better and was thus adopted as standard method.

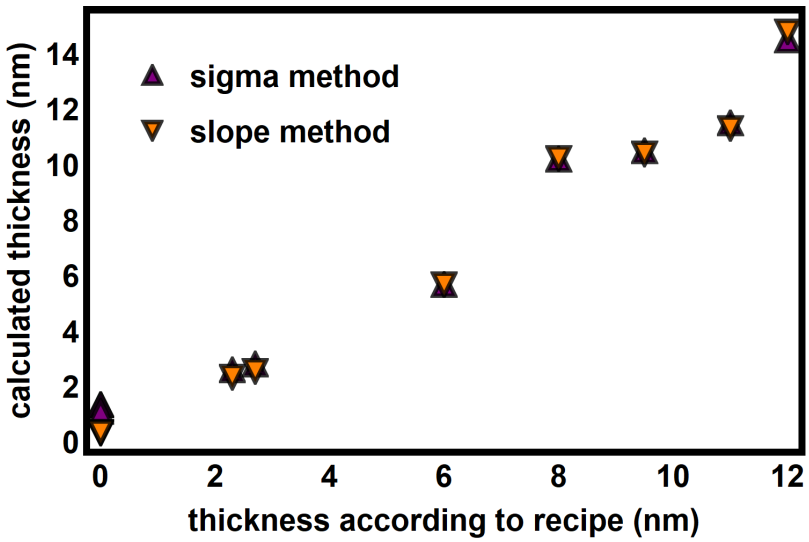

Figure 19: **Comparison of XPS peak fitting approaches**
Results for the slope and sigma method applied on our XPS data. In general both approaches deliver almost the same results. Slight differences occur at around 0 nm and 12 nm

3.2.3.3 Combining ellipsometry and XPS

We compare XPS and ellipsometry (Figure 20). The results show that the two techniques agree well for a thickness range of 2 nm-6 nm. For larger thicknesses, the discrepancy increases, which is related to fact that the XPS method only works well for thin layers. This information led us to the conclusion that ellipsometry can be used down to 2 nm, while XPS can be used from 0 nm-6 nm.
Now we can investigate the reproducibility of the desired SiO_2-layer thickness grown with the RTA device. Figure 21 shows that the deviation between different RTA runs with the same growth recipe is small, especially for the range between 2 nm and 8 nm. Given the reproducibility with the RTA we assumed for the rest of the project that the grown thickness was an average of thicknesses previously obtained from the same growth recipe.

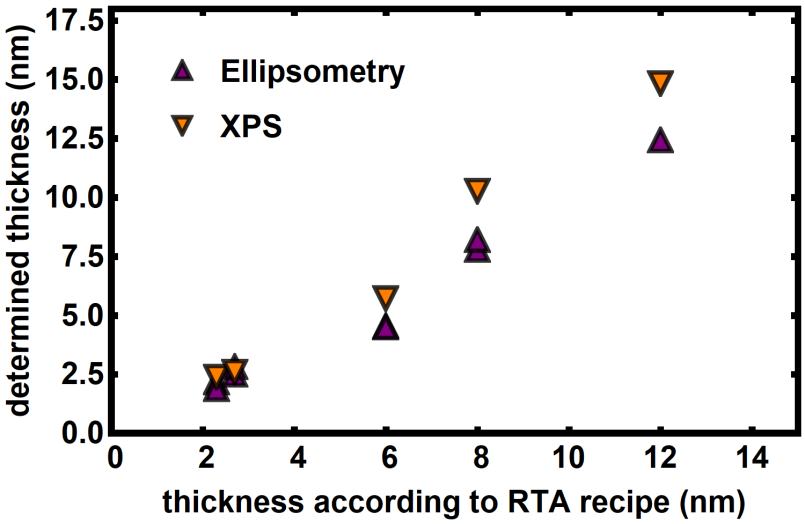

Figure 20: **Ellipsometry vs. XPS**
The two methods show good agreement for small thicknesses, while the measured values diverge away from each other with increasing thickness.

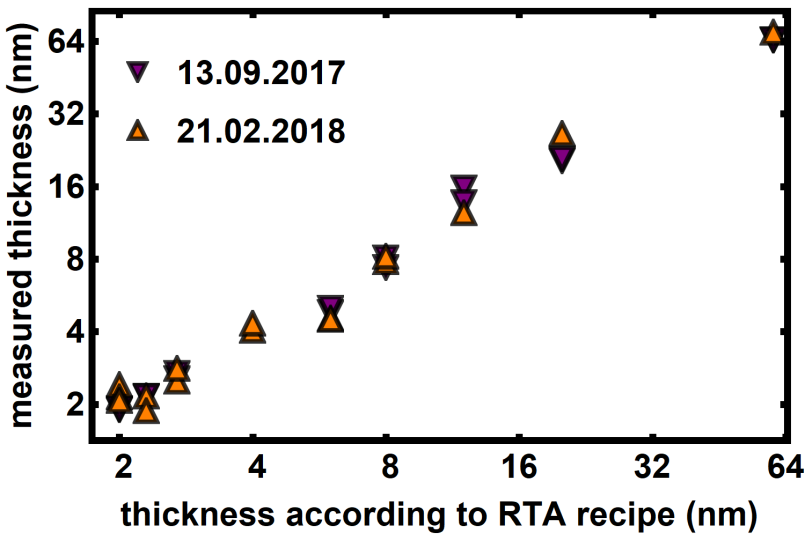

Figure 21: **RTA reproducibility**
Thickness measurement data for two different RTA-runs. The discrepancy of the values increases with thickness, which does not become clear from the figure because it is a log-log plot.

3.3 PbS QD deposition on Si/SiO$_2$

The initial goal for the QD deposition was to obtain sub-monolayer coverage, with an inter-QD separation of around 20 nm by 20 nm. This would prevent the QDs from interacting with each other[32] and would also correspond to the intended final solar cell geometry. However, such a coverage is too low to produce a detectable PL signal and as a result a coverage of a few QD layers was used. This means that the QDs interact with each other, which might lead to additional PL quenching due to an increased likelihood that surface traps are encountered during inter-QD energy transfer. However, this loss process should not be affected by the distance of the interacting QDs to the Si substrate, and thus should not affect our measurement of the lifetime over distance curve.

3.3.1 Spincoating

Two deposition methods were initially considered, drop-casting and spin-coating. Early trials showed that drop-casting of the solution onto the substrate led to visible localized agglomerations of QDs. Spin-coating proved to result in a homogeneous coverage, as seen with scanning electron microscopy (SEM) (see Subsection 2.1.4). If not stated otherwise, the following spin-coating parameters were used throughout this thesis: After deposition of 50 µl of a 5 mg ml^{-1} QD solution, the spin-coating was done with a ramp-up time of 1.5 s, a dwell time of 10 s and a rotational frequency of 1500 RPM during the dwell time.
The QDs used for the lifetime measurements later on had bandgaps between 1.2 eV and 1.5 eV, which corresponds to QD sizes between 3.4 nm and 2.6 nm, respectively. It is not possible to resolve those sizes via SEM and thus, in order to get a better picture of the QD arrangement, SEM was performed on 0.7 eV PbS QDs, corresponding to 7.4 nm in size. The coverage of the QDs was varied by changing the concentration of the QD solution, which led to coverages ranging from 1-2 layers to sub-monolayer coverages in the range of the 50 nm by 50 nm QD separation, which we had intended to use initially. Figure 22 shows these coverages for different QD concentrations. We assume similar coverages for 1.2 eV and 1.5 eV quantum dots with the same concentrations.

3.4 TCSPC setup

The lifetime measurements where conducted using a time-correlated single photon counting setup (TCSPC). Figure 23 illustrates the beam path and important elements that were used for the measurements. Two pulsed lasers, one at 640 nm (PicoQuant LDH-D-C-640) and the

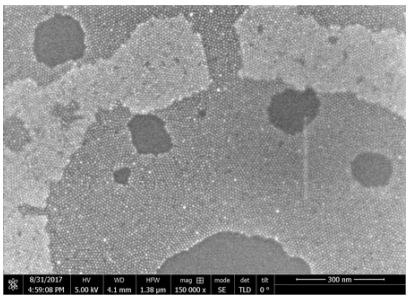

(a) **10 mg ml^{-1}**

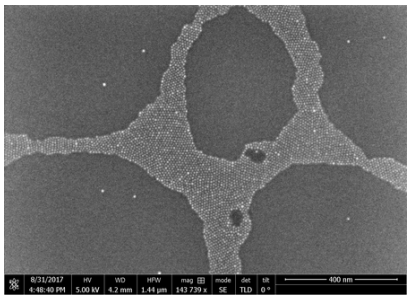

(b) **4 mg ml^{-1}**

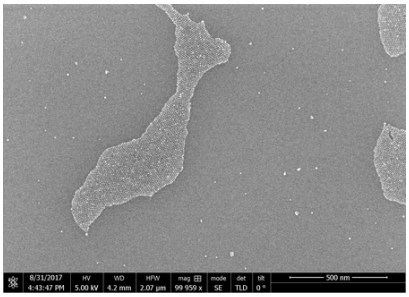

(c) **0.8 mg ml^{-1}**

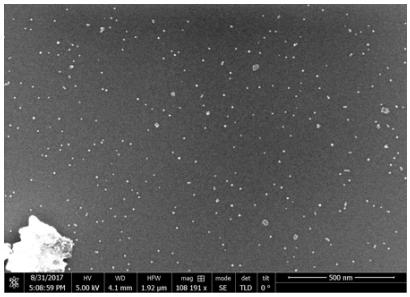

(d) **0.2 mg ml^{-1}**

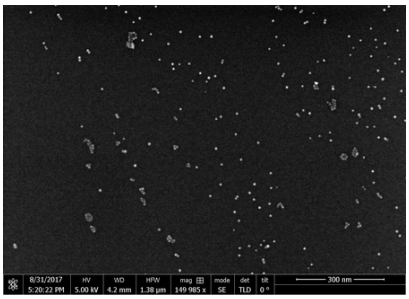

(e) **0.05 mg ml^{-1}**

Figure 22: **QD coverages for different QD concentrations in solution**
The figures illustrate how the coverage goes down the more dilute the spin-coated solution is. The scale bar is located at the bottom right of every figure. SEM images were taken with a FEI Verios 460 SEM system using a through the lens detector (TLD).

other one at 485 nm (PicoQuant LDH-D-C-485), were available for the measurements. Unless otherwise stated, the blue laser was used to obtain the data shown in this thesis. The repetition rate of the laser is controlled by a "PicoQuant PDL 828 Sepia II". The laser is coupled into the beam path where neutral density (ND) filters and a power meter can be flipped in to change and measure the laser power. After reflection from a dichroic mirror, the light is focused onto the sample via a water immersion objective. A 20 µl demineralized water droplet is deposited between the objective and a glass cover slide to increase the system numerical aperture of the system. The substrate lies on top of that cover slide, facing downwards towards the light beam. Due to the limited working distance of the objective, the cover slide needs to have a thickness of 200 µm or less. When the laser light reaches the substrate, part of it is absorbed by the substrate and part of it is reflected. The light absorbed by the sample is for the biggest part used for the excitation of the QDs on the sample. The subsequently emitted radiation by the QDs along with the reflected laser light is directed towards either a CCD-camera or towards a single photon avalanche diode detector (SPAD) (Micro Photon Devices, MPD-5CTD). The laser light is filtered out in the detector path by a combination of a long pass and a notch filter (ET500LP and ZET488NF, both from Chroma), so that only the light emitted by the QDs can reach the detector.

3.4.1 Focusing

A piezo-stage allows for changing the distance between the sample and the objective. In combination with the CCD camera, this is usually used to focus the laser beam onto the sample surface. However, for the QD PL lifetime measurements, low repetition rates (0.1 MHz) are used, which means that the PL signal from the QDs is less intense and thus difficult to detect with the CCD camera. In principle, one could just use higher repetition rates or even the continuous wave mode to focus and then switch back to a lower repetition rate. In Subsection 3.6.2 it will become clear that this should be avoided due to photo-degradation of the QDs. We circumvent this issue by maximizing the amount of photons detected by the SPAD, by scanning the relevant objective-sample separation range with the piezo-stage.

3.4.2 Encapsulation

The setup shown in Figure 23 is the standard arrangement which was used in the beginning of the project. Upon realization that degradation in air is a major issue, the setup was upgraded with encapsulation, which allows for storage of the samples in a nitrogen environment during the measurement (Figure 24). The encapsulation consists of a stainless steel main chamber that has two openings. A cover slide

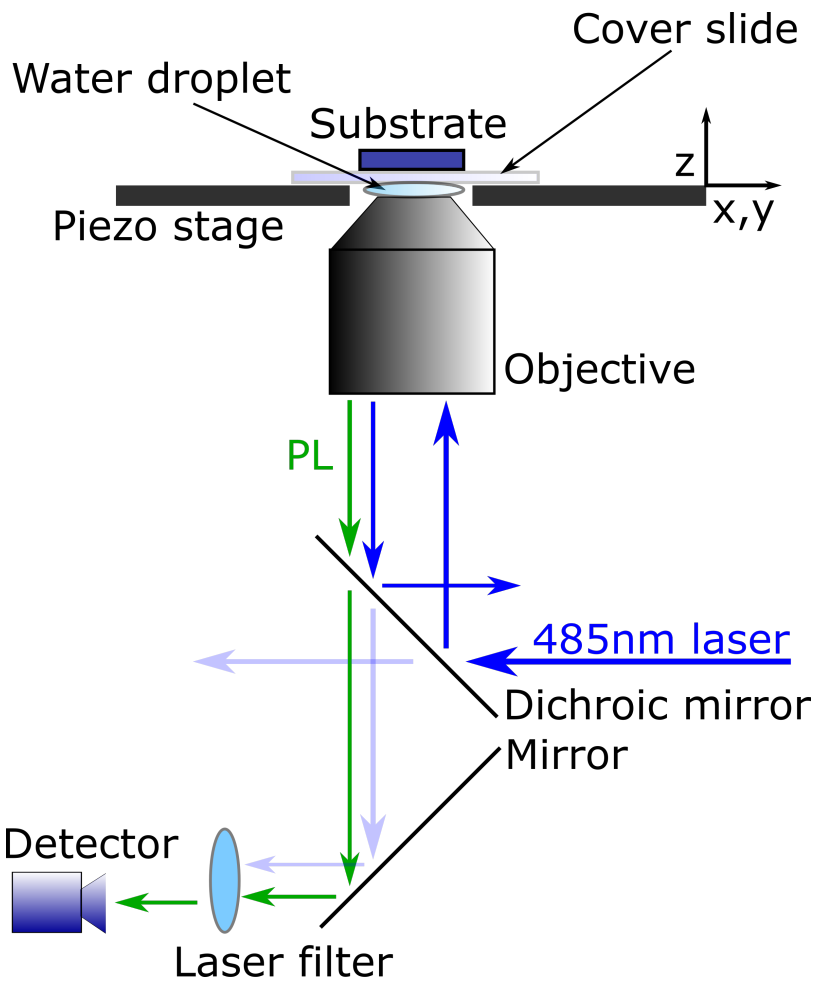

Figure 23: **TCSPC setup**
For the main measurements the substrate is encapsulated as in Figure 24 and an additional mirror can be flipped in between the two mirrors shown to direct the light towards a CCD.

is glued onto the front opening with silicate glue and the back side can be closed with a stainless steel plate that is screwed onto the back of the main chamber. To make the interface between the main chamber and the back plate air-tight, a small groove with an O-ring was added to the main chamber. With this encapsulation we can load the sample in the glove box environment and measure it afterwards by putting the encapsulation onto the objective plus water droplet with the cover slide window facing downwards.

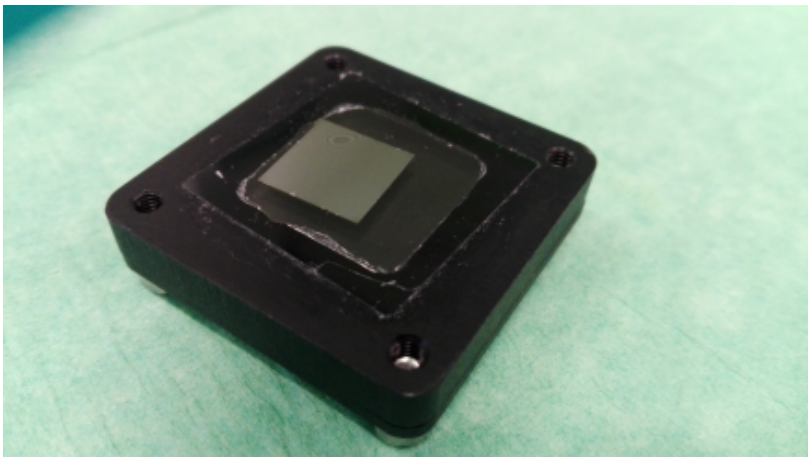

Figure 24: **Sample encapsulation**
The QD on Si sample is enclosed in the encapsulation out of stainless steel under N_2-environment and slight overpressure. The front window is a thin glass cover slide.

3.5 Data collection and processing

3.5.1 Data collection

In general, the TCSPC measurement provides a dataset in the shape of an image that contains information on the total amount of photons counted as well as a counted photons over time histogram for every pixel. This allows for comparison of lifetimes between different regions. It also allows to distinguish between regions with intense PL and less intense/no PL. This is a useful tool, as the homogeneity of the QD film can be determined by checking how much the PL differs across the imaged region. In general, strong inhomogeneities are not observed apart from QD agglomerations around the occasional dust particle or at the sample edges. Differences in lifetimes for strongly inhomogeneous regions are observed, although these differences are probably not physical but related to the dead-time of the detector, as will be explained in detail in Subsection 3.6.1. The most consistent and comparable way of measuring lifetimes and photon counts is to measure regions with high homogeneity, which can be found for every sample.

3.5.2 Data processing

While the image is used to check the surface structure for homogeneity, the histogram provides all the information needed for the following analysis. The total photon counts can be determined by integration over the whole curve, and the lifetimes by applying a proper fitting model to the curve.

3.5.2.1 PL-decay fit model

While the PL of QDs in solution shows a bi-exponential decay[69], this is not the case after deposition (Figure 25). To obtain the best fit function, three different functions can be considered. These are a biexponential, triexponential, and a stretched exponential function, with 5,7 and 4 free fit parameters, respectively. It turns out that the fit accuracy strongly improves from bi- to triexponential and is also quite high in the case of the stretched exponential. In principle, this would lead to the conclusion that the stretched exponential is the best choice, as it optimizes the fitting accuracy against amount of required fitting parameters. However, stretched exponential functions are not favorable as one cannot easily draw conclusions with respect to the physics behind the decay. Contrary to that, using a triexponential decay function allows for division of the decay function into three distinct mathematical terms, which can correspond to three distinct physical processes with individual lifetimes and amplitudes. Taking this into account, we will use the triexponential function for the data analysis from now on. This means that every dataset will provide three different lifetimes along with corresponding amplitudes and a background (Equation 16).

$$PL(t) = \sum_{i=1}^{3} A_i * e^{-\frac{t}{\tau_i}} + PL_0 \tag{16}$$

...where...

PL	photoluminescence lifetime
t	time
A_i	amplitudes
τ_i	lifetimes
PL_0	background signal

3.6 Determination of the optimal measurement conditions

In order to obtain reproducible, trustworthy data all possibly influential parameters need to be known and detrimental effects taken into account or eliminated. In the following, the TCSPC setup and the QD-Si samples are checked for such cases.

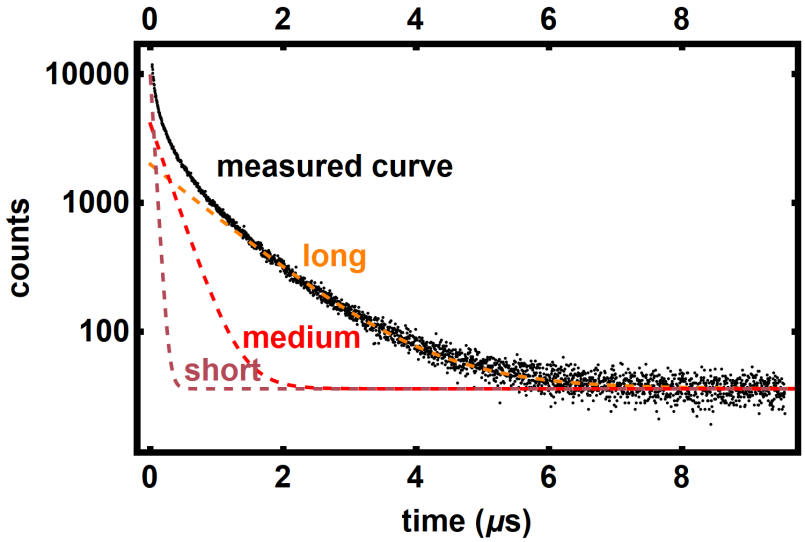

Figure 25: **Example of PL decay fitting**
The measured PL decay data (black) is plotted along with the three exponential functions obtained from fitting. The labels of the curves indicate the time scale of the individual decays as used throughout this thesis.

3.6.1 TCSPC: possible sources for errors

The TCSPC setup contains a SPAD detector, which has a dead time of 90 ns[70]. This means that after the detection of a photon, the detector needs 90 ns before it can detect another photon. For an exponentially decaying signal, where most, but not all photons will reach the detector shortly after the initial excitation, this means that photons in the early stages of the decay are more likely to be counted than later ones, as the the diode will be "dead" for 90 ns after the first photon. This effect is especially detrimental when the time scale of measurement is of the same order as the dead time of the SPAD, as then only one photon can be detected, which in most cases will be a photon from the early stage of the decay. The longer the measurement time in comparison to the dead time, the more minute this effect becomes, as more dead times fit into the time range of the measurement. A low photon countrate can also be helpful, as it decreases the likelihood of detecting two photons in one laser pulse cycle. This is called the "Pile-up"[70] effect and leads to a systematic underestimation of lifetimes. According to literature[70], the rule of thumb is to have a photon count rate of 5% of the laser repetition rate or less. For our measurements, we have a repetition rate of 100 kHz, which corresponds to a measurement time of 10 µs and thus around 111 dead times, which in principle should give enough counts for later photons. However, as Figure 26 indicates, the measured lifetimes strongly depend on the photon rate received at the detector. The data points are obtained by changing the excitation density of the sample by varying the ND

filters in the light path. We see the change of all three lifetime components as a function of overall counts on the left and the change of the amplitudes as a function of overall counts on the right. The errorbars are large for fewer counts, because the fitting algorithm loses precision. The amplitudes of the fitting function increase with the number of collected photons. We observe a lifetime peak in the range of $0.2 \cdot 10^6 - 1.2 \cdot 10^6$ photon counts. This functional behavior could either mean that we indeed see the influence of the dead time of the SPAD or that the lifetimes depend on the excitation density. In order to be able to distinguish between those two possible causes, a similar measurement series, where the excitation density is kept constant but the signal attenuation right in front of the SPAD is varied, needs to be done. Should we still see the same behavior, we can conclude that it is caused by the detector, otherwise it is most likely related to the excitation density.
In order to make the measurements consistent with each other, the photon count rate given by the detector should be about the same for every measurement. The acceptable range of count rates according to Figure 26 lies between 1500 and 2500 counts per second (shaded region), which is what we adjust the setup to for every measurement.

3.6.2 QD-Si sample degradation

QD-Si samples suffer from considerable degradation over time. One way to passivate the sample would be by spin-coating PMMA onto it. However, the PMMA solvents we tried appear to interact with the underlying QD layer, thus dissolve and mix it with the PMMA, which is undesirable for our purposes. Another option is encapsulation of the samples during the measurement, which is the path we took for our measurements (Subsection 3.4.2). However, as Figure 27 shows, not even this measure can provide complete protection from degradation, for two reasons: The encapsulation seems to be not completely air-tight. The detrimental part about contact with air is the oxygen, which, when in contact with the QDs, can form PbOx[62] that acts as a trap state. Another reason why the encapsulation does not fully prevent degradation is that the QDs are also sensitive to light, which means that they are subject to photo-degradation[62]. Similarly to the minor exposure to oxygen, exposure to light cannot be prevented either, as the lifetime measurement itself relies on photo-excitation of the sample (see Figure 27). In general, the photo-degradation due to ambient light sources is weaker than the degradation due to oxygen. During the measurement photo-degradation is much stronger due to the high-intensity irradiation.
The overall degradation can be described by a combination of two physically distinct processes. One is (photo-assisted) oxidation and the other one is photo-induced sintering[62]. Oxidation of Pb to PbO

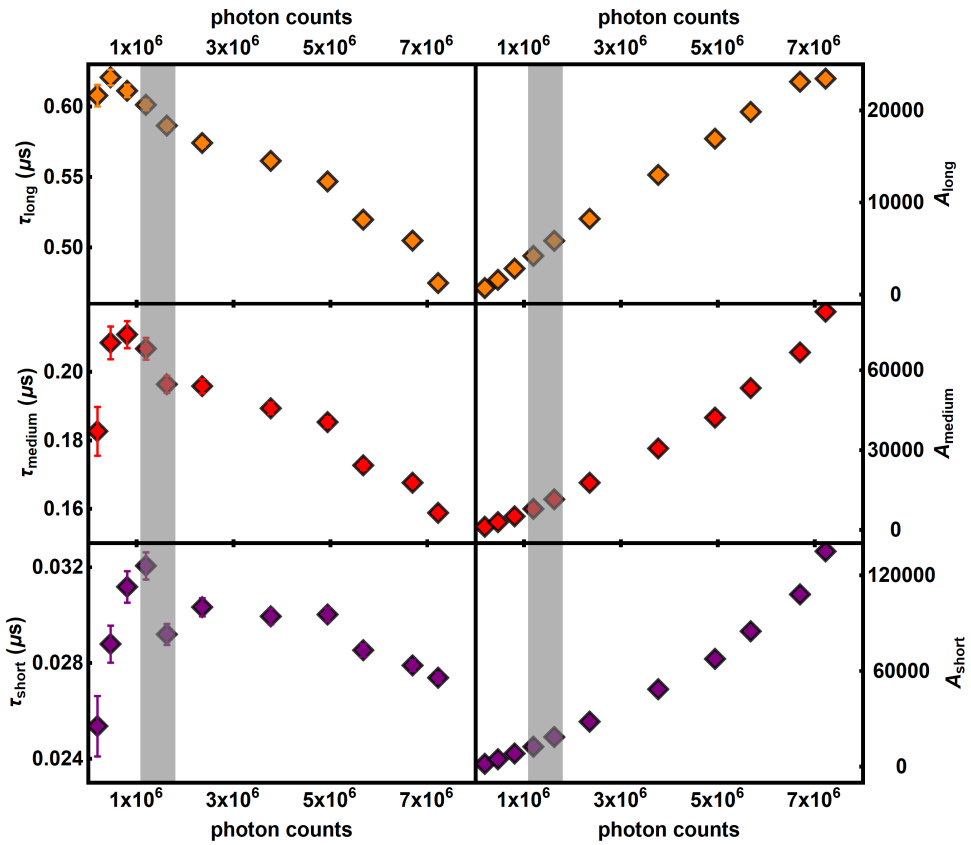

Figure 26: **Lifetime as function of photon counts**
The figure shows the dependence of the three lifetime components (left) and the corresponding amplitudes (right) on the number of detected photons. The shaded area marks the allowed photon count region for the measurements that follow.

or $PbSO_4$ happens as long as there is O_2 available in the environment. The oxidation can be accelerated by photo-exposure, as excitation of the QDs means that there are additional charge carriers which can contribute to a charge carrier assisted oxidation process[62]. Photo-exposure also heats the system via non-radiative decay processes. This leads to sintering[62] of the PbS QDs to create QDs of bigger sizes.

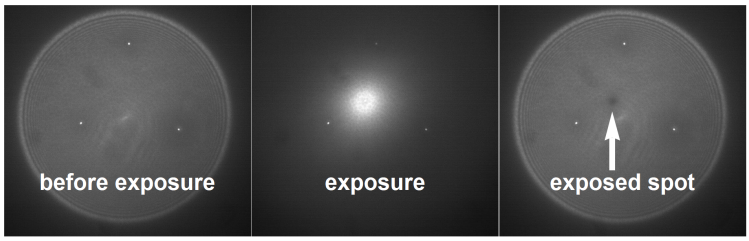

Figure 27: **Photodegradation of the QD layer**
The first panel shows a CCD image of the QD layer before exposure. The three white dots correspond to dirt particles around which the QD density is higher. In the middle we see an image of the same area, but with the laser focused onto a small spot. After focusing, the same image as in the first panel appears, but the spot where the laser was focused appears darker than the surrounding area.

Figure 28 illustrates the two different degradation mechanisms, as three different regions on the same sample are measured consecutively. Each region is measured three times in a row, with a single measurement lasting around 12 min. Two physically distinct degradation slopes can be identified from the graph.
One of them connects the first measurement at every region. The regions differ in the amount of time they were exposed to air that found its way into the encapsulation chamber, by about 36 min each. This means that the comparison allows to determine a degradation slope due to exposure to air.
A steeper slope can be identified for the comparison of the measurements at the same spot. In this case, the sample is affected by both degradation processes, which means that the difference between this slope and the slope due to air exposure is the photo-degradation slope for our measurements. Table 2 shows that the slopes of the two degradation processes identified are in the same order of magnitude. This means that the encapsulation suppresses the oxidation due to air strongly enough such that other, photo-induced processes become important as well. As the PL lifetime measurements rely on photo-excitation, the photo-degradation process cannot be eliminated, which means that this order of magnitude for the degradation slope is the limit of what we can reach with our encapsulation.

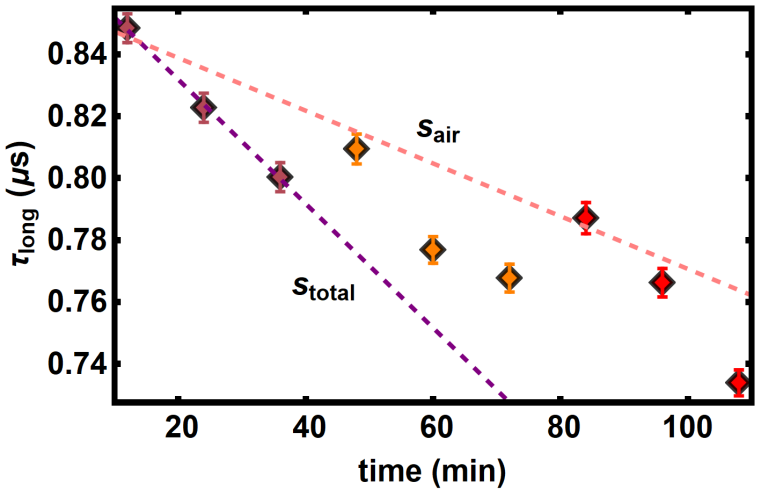

Figure 28: **PL lifetime degradation over time**
The graph shows the change of the long lifetime component over time. Three measurements were taken at three different spots. Measurements at the same spots are marked in the same color. The fitted degradation slopes are plotted as dashed lines and the values of the slope can be found in Table 2

Table 2: **Degradation slopes determined from Figure 28**
s... degradation slope with corresponding error Δs
s_{tot}... combined degradation slope
s_{enc}... degradation slope due to air
s_{ph}... photo-degradation slope

slope	s (μs min^{-1})	Δs (μs min^{-1})
s_{tot}	−2.0	0.3
s_{enc}	−0.9	0.1
s_{ph}	−1.1	0.4

4 RESULTS & DISCUSSION

4.1 First indications of quenching of the QD PL

QDs in a solution of 5 mg ml^{-1} are spin-coated onto a Si sample with native oxide and a quartz sample. The quartz sample has received the same sample preparation as usual for Si. The comparison of the lifetimes of Si and quartz (Figure 29) shows that the PL-lifetime of the QDs on Si is quenched compared to the quartz sample, which can be regarded as a first indication of energy transfer from the QDs into Si. Furthermore, the QD coverage on quartz looks far less homogeneous than for QDs on Si, which is due to scratches on the quartz surface.

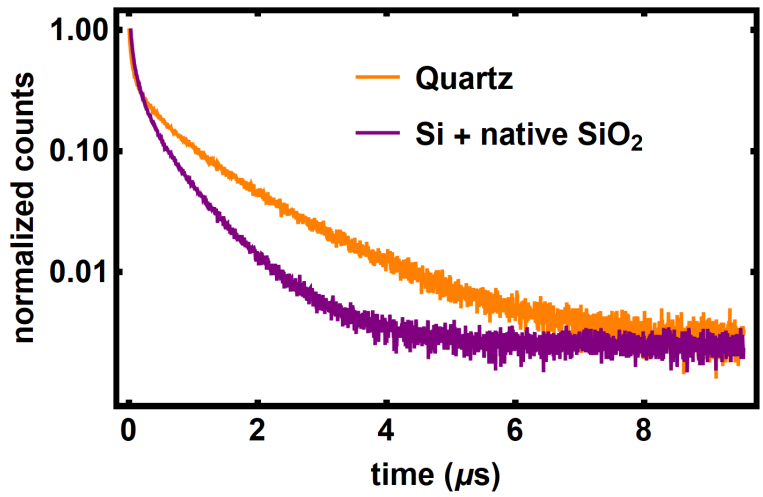

Figure 29: **Quenching of PbS QD PL on Si**
Normalized PL decay over time for QDs on quartz substrate and on a Si substrate covered with 1.9 nm of native SiO_2. The decay curves show a similar trend for the first 200 ns. Afterwards, the PL of the QDs in proximity of Si decays faster.

4.2 PL lifetime as a function of donor-acceptor separation

We can now look at the PL-lifetimes as a function of QD (donor) - Si (acceptor) separation. Figure 30 shows that the PL decay rate is decreasing as the donor approaches the acceptor. This trend becomes unambiguous for SiO_2 thickness below 6 nm.
The long decay rate k_{long} shows a change of the FRET efficiency from zero to up to 28 % at the smallest separation (0.4 nm). k_{medium} and

k_{short} show lower maximum efficiencies of 17 % and 12 %, respectively.
For all three rates we observe a rate minimum around 27 nm and a subsequent increase of the rate with increasing distance.
The two shorter rates seem to agree better with the model than k_{long}. One reason for that is that the errorbars appear to get bigger for the shorter rates. However, this only appears to be the case due to the fact that the relative change of the rates over the whole distance range decreases, meaning that the errors span over a larger part of the y-axis. In fact, the relative errors of all three rates are about the same.
To get the modeled curve, the Förster distance has to be calculated for 1.5 eV QDs, which means that they have a PL emission centered around 1.35 eV, due to the Stokes shift[35]. The value for the QY is the only fitting parameter used for the curve. This gives $R_0 = 1.14\ nm$, which corresponds to a QY of 0.1. The base lifetime $\tau_{D,0}$ is taken to be the average of the rates at 13.5 nm and 27 nm. The comparison with the data shows good agreement of theory and experiment.

4.3 FRET efficiency

This section describes the FRET efficiency we achieved with our geometry. As we have three different rate components, of which all change as a function of distance, we have to combine them. The most straightforward way to do this is by calculating the individual FRET efficiencies and weighing them with the amplitudes of each component. By doing so, one accounts for the amount of photon events that can be attributed to each of the decays. This is done according to Equation 17 and shown in Figure 32.

$$\eta_{FRET} = \frac{\sum_i \eta_i \cdot A_i}{\sum_i A_i} \tag{17}$$

... with ...

η_{FRET}	weighted FRET efficiency
η_i	FRET efficiencies
A_i	fitted decay amplitudes

4.4 Discussion

It's worth noting that similar distance dependencies can be found for all three rate components, although the distance dependence is weakened towards the shorter components. This means that the highest FRET efficiency values can be found for the long decay rate k_{long}. The question about how to interpret the different efficiencies for the different components is addressed in Section 4.3.

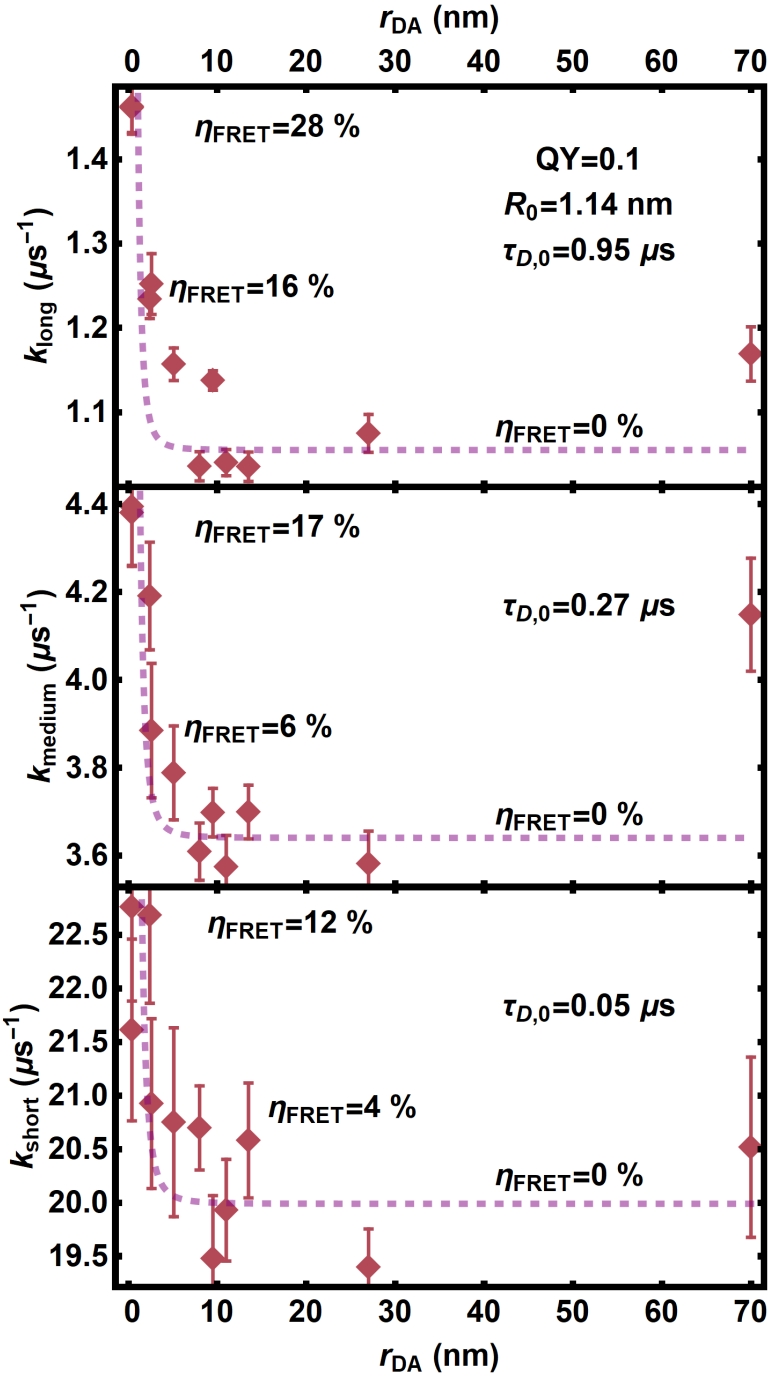

Figure 30: **PL decay rates as function of distance**
The figure shows the distance dependence of all three decay rates. The errorbars represent the error of the mean of three consecutive lifetime measurements at three different spots each. The purple line corresponds to the model, with Q_D as fit parameter. FRET efficiencies are indicated for comparison between the different components.

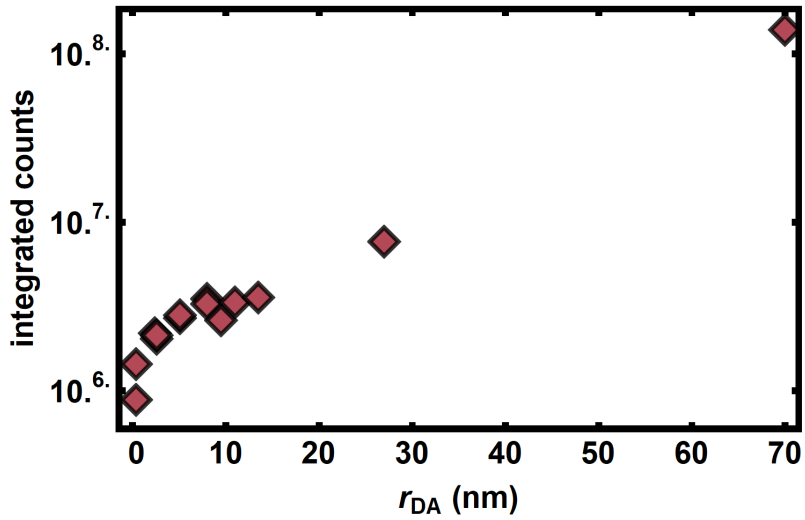

Figure 31: **Photon counts as function of distance**
The photon counts increase with increasing separation between the QDs and Si.

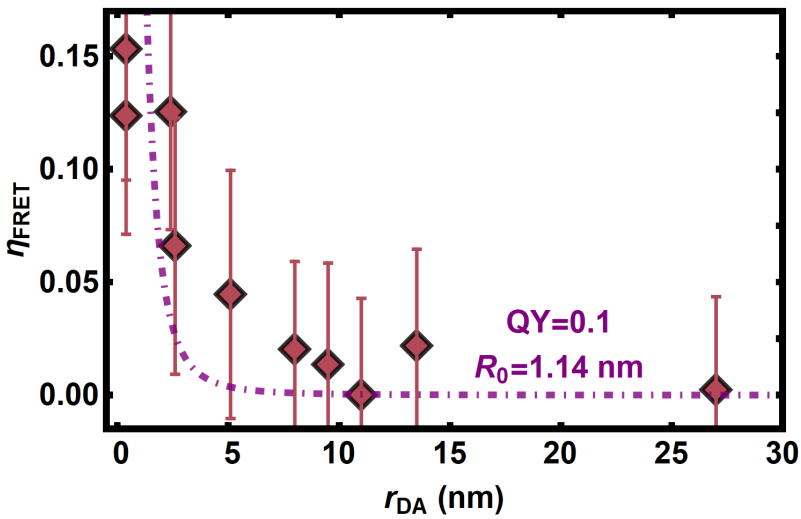

Figure 32: **FRET efficiency**
The points represent the efficiencies obtained by weighing the three different efficiency components with the corresponding amplitudes (Equation 17). This gives a maximum FRET efficiency of $\eta_{FRET} = 15.3$ % at 0.4 nm. The purple, dashed line represents the model with Q_D set to 0.1.

What is striking is that the weighed FRET efficiency seems to be dominated by the efficiency obtained from the short rate component, as the values are rather close to each other. This is due to the fact that the amplitudes are the smallest for the long decay rate and the highest for the short one. It also makes sense that the efficiency can be fitted with the same values as the rates, because it is base rate independent and all three components fitted the same curve quite nicely as well. The errorbars are large, which results from error propagation throughout the calculation of the efficiency from the rates and subsequent weighing. We note that our geometry exhibits a maximum measured FRET efficiency of $\eta_{FRET} = (15.3 \pm 6.1)\%$ at a separation of 0.40 nm and according to the model curve 90.0 % efficiency should be reached at 0.37 nm, and with a quantum yield of 100 %, we would reach 98.7 % efficiency at 0.4 nm. However, from Figure 32 it becomes clear that the data points do not agree well with these two predictions. This is related to the x-error of the data points, as small deviations along the r_{DA}-axis cause big changes in the predicted rate and subsequently lead to discrepancies between experiment and model.

The rates at 70 nm separation (Figure 30) indicate that the rate rises again for larger separations, which can be observed for all three components. This trend may be due to the so-called local density of optical states (LDOS), that changes as a function of distance. The LDOS determines how many available states there are for the radiation of photons, with a high value meaning that photons can be emitted at a faster rate. This means that, although the measured rate increases, it does not necessarily mean that the rate of energy transfer towards Si increases, but only that more photons are emitted per unit time. Such a consideration can be supported by taking a look at photon counts as a function of distance, as shown in Figure 31. If the higher rate would be caused by energy transfer directly into Si, then one would expect that the number of photon counts would also decrease, as more of them would be directed towards the acceptor. However, we observe a steady increase of photon counts over distance, which indicates that the LDOS changed in such a way that more photons are emitted at a faster rate. Another phenomenon that could be part of the explanation is that the out-coupling efficiency increases with increasing separation from Si.

The length scale at which we see considerable change in the rates appears to be of the same order as the characteristic length scale for Dexter energy transfer (<1 nm), suggesting that a Dexter model could also describe the same data set. The treatment of this question can be found in Subsection 4.4.1, along with a comparison to the ordinary point acceptor FRET model.

4.4.1 Comparison with other models

While Figure 32 serves as a strong indication for energy transfer, it does not reveal the mechanism responsible. Throughout this thesis we assumed that FRET is the responsible mechanism, but we now consider other options. The most likely mechanism that could be responsible for our observations, apart from FRET, is Dexter energy transfer. In order to obtain the curve for Dexter energy transfer, some parameters for the DET rate (k_{DET}) have to be defined first (Equation 18).

$$k_{DET} = K \cdot J_{DET} \cdot e^{\frac{-2r_{DA}}{L}} \tag{18}$$

...where J_{DET} is the normalized spectral overlap integral (Equation 19), L the sum of the van der Waals radii of donor and acceptor and K an experimental factor. The van der Waals radius of a QD is difficult to determine as it is defined as the closest approach distance for an atom. In absence of a definition for the case of QDs, we assume it is equal to half the QD size ($L = L_{Si} + L_{QD} = (0.21^{71} + 1.31)\ nm = 1.52\ nm$).

$$J_{DET} = \int_0^\infty \overline{f_{QD}(\lambda)} \cdot \overline{\alpha_{Si,M}(\lambda)} \lambda^4 d\lambda \tag{19}$$

...where $\overline{\alpha_{Si,M}(\lambda)}$ is the normalized molar absorption coefficient of Si. The normalization of the molar absorption coefficient is the only difference between J_{DET} and the J we introduced in Subsection 2.1.3. Figure 33 compares the best fit for DET with a FRET bulk model fit and a FRET point model fit. What becomes apparent is that the bulk and point models describe similar curves, indicating that the quality and quantity of our measured data does not allow us to distinguish between a 3rd and 6th power dependence. The Dexter curve follows a different trajectory but does not differ too much either. The reason why DET is actually able to replicate our data points, although they should be beyond the relevant distance for DET, is the big van der Waals radius we assumed for our system. Usually, van der Waals radii are in the order of a few Ångstrom, but here we assume the van der Waals radius for the QDs to be 1.31 nm, which is far bigger. This relaxes the strong distance dependence of DET (see Equation 18).
As apparent in Figure 33, our data cannot distinguish which transfer process is happening. In the end, it could be a superposition of both mechanisms.

4.4.2 Future work

The most important step that needs to be taken towards the realistic system is the remeasurement of the efficiency curve (Figure 32) for

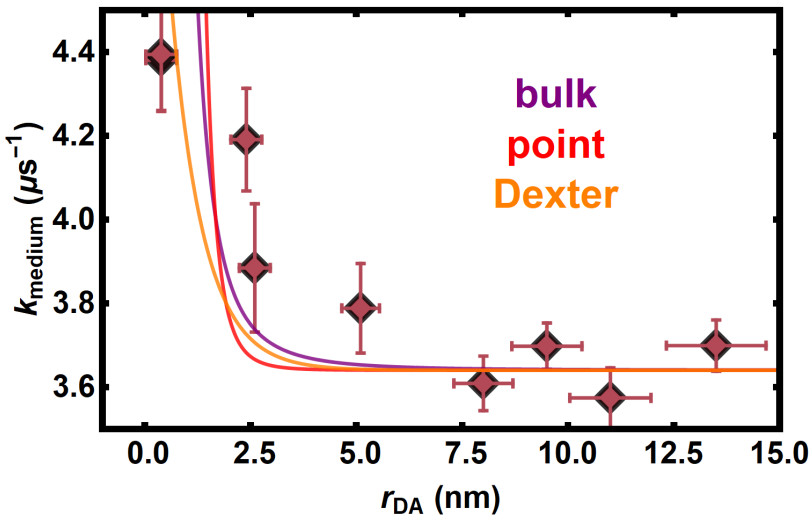

Figure 33: **Comparison between FRET and DET**
For the comparison we use the medium rate component. We can rates for the bulk, point and DET model, with all three functions following similar trajectories through our data points. The x-errors represents the larger value of either maximum relative error measured in Figure 16 or the absolute error for the smallest measured thickness value of Figure 16.

1.2 eV QDs. This would finally answer the question if our geometry works for singlet fission enhanced solar cells.
Secondly, in the case of successful energy transfer, the full geometry should be assembled and IQE measurements conducted in order to check for changes compared to an ordinary solar cell. From there on, optimization will be necessary (QD-coverage, Tc-layer thickness, deposition method,...) to obtain the most efficient solar cell sample.
Further investigations to distinguish FRET from DET could be done by measuring the QY of the QDs. With this, there would be no fitting parameter left in the FRET equations, and if the data and model still agrees by then, this would be a strong indication for the validity of the FRET model. Additionally, more data points with smaller error bars need to be measured. According to Figure 33, to be able to conclusively assign a model to the data, the relative errors of the data points need to be less than 8.0 % for r_{DA} (x-error) and 0.3 % for the rate (y-axis).
It might also make sense to switch away from PbS QDs towards other QDs, as the strong Stokes shift of PbS QDs puts a large constraint on the bandgap and emission range.

5 SUMMARY

To summarize, we introduced a new singlet fission solar cell geometry (Figure 4 and Figure 5) which could achieve high efficiencies, provided that the energy transfer from PbS quantum dots to Si is sufficiently efficient. We assumed that this transfer step is mainly governed by the Förster resonant energy transfer and introduced an extension to the commonly used Förster formalism, which assumes a bulk acceptor (Equation 12). Our theoretical predictions show efficient transfer at a donor-acceptor separation of less then 5 nm (Figure 12), which we could confirm experimentally (Figure 30). We find energy transfer efficiencies of up to 15.3 % (Figure 32), depending on the distance. However, we cannot rule out that a different transfer mechanism, such as Dexter energy transfer, could be responsible for our observations (Figure 33).

BIBLIOGRAPHY

1. The kyoto protocol. https://unfccc.int/process-and-meetings/the-kyoto-protocol/what-is-the-kyoto-protocol/what-is-the-kyoto-protocol. Accessed: 2018-07-11.

2. The doha amendment. https://unfccc.int/process/the-kyoto-protocol/the-doha-amendment. Accessed: 2018-07-11.

3. The paris agreement. https://unfccc.int/process-and-meetings/the-paris-agreement/the-paris-agreement. Accessed: 2018-07-11.

4. Swanson Richard M. A vision for crystalline silicon photovoltaics. *Progress in Photovoltaics: Research and Applications*, 14(5):443–453.

5. G. E. Moore. Cramming more components onto integrated circuits. *Proceedings of the IEEE*, 86(1):82–85, Jan 1998.

6. G. E. Moore. Progress in digital integrated electronics [technical literaiture, copyright 1975 ieee. reprinted, with permission. technical digest. international electron devices meeting, ieee, 1975, pp. 11-13.]. *IEEE Solid-State Circuits Society Newsletter*, 11(3):36–37, Sept 2006.

7. Kunta Yoshikawa, Wataru Yoshida, Toru Irie, Hayato Kawasaki, Katsunori Konishi, Hirotaka Ishibashi, Tsuyoshi Asatani, Daisuke Adachi, Masanori Kanematsu, Hisashi Uzu, and Kenji Yamamoto. Exceeding conversion efficiency of 26interdigitated back contact solar cell with thin film si technology. *Solar Energy Materials and Solar Cells*, 173:37 – 42, 2017. Proceedings of the 7th international conference on Crystalline Silicon Photovoltaics.

8. Green Martin A., Emery Keith, Hishikawa Yoshihiro, and Warta Wilhelm. Solar cell efficiency tables (version 37). *Progress in Photovoltaics: Research and Applications*, 19(1):84–92.

9. Seok Sang Il, Graetzel Michael, and Park Nam-Gyu. Methodologies toward highly efficient perovskite solar cells. *Small*, 14(20):1704177.

10. M P Suryawanshi, G L Agawane, S M Bhosale, S W Shin, P S Patil, J H Kim, and A V Moholkar. Czts based thin film solar cells: a status review. *Materials Technology*, 28(1-2):98–109, 2013.

11. A De Vos. Detailed balance limit of the efficiency of tandem solar cells. *Journal of Physics D: Applied Physics*, 13(5):839, 1980.

12. Tayebeh Ameri, Gilles Dennler, Christoph Lungenschmied, and Christoph J. Brabec. Organic tandem solar cells: A review. *Energy Environ. Sci.*, 2:347–363, 2009.

13. L. Tsakalakos, J. Balch, J. Fronheiser, B. A. Korevaar, O. Sulima, and J. Rand. Silicon nanowire solar cells. *Applied Physics Letters*, 91(23):233117, 2007.

14. Erik Garnett and Peidong Yang. Light trapping in silicon nanowire solar cells. *Nano Letters*, 10(3):1082–1087, 2010. PMID: 20108969.

15. A.J Nozik. Quantum dot solar cells. *Physica E: Low-dimensional Systems and Nanostructures*, 14(1):115 – 120, 2002.

16. V. Aroutiounian, S. Petrosyan, A. Khachatryan, and K. Touryan. Quantum dot solar cells. *Journal of Applied Physics*, 89(4):2268–2271, 2001.

17. W. Shockley and H. J. Queisser. Detailed Balance Limit of Efficiency of p-n Junction Solar Cells. *Journal of Applied Physics*, 32:510–519, March 1961.

18. Yuen Yap Cheng, Burkhard Fueckel, Rowan W. MacQueen, Tony Khoury, Raphael G. C. R. Clady, Tim F. Schulze, N. J. Ekins-Daukes, Maxwell J. Crossley, Bernd Stannowski, Klaus Lips, and Timothy W. Schmidt. Improving the light-harvesting of amorphous silicon solar cells with photochemical upconversion. *Energy Environ. Sci.*, 5:6953–6959, 2012.

19. J. de Wild, A. Meijerink, J. K. Rath, W. G. J. H. M. van Sark, and R. E. I. Schropp. Upconverter solar cells: materials and applications. *Energy Environ. Sci.*, 4:4835–4848, 2011.

20. T. Trupke, M. A. Green, and P. Wuerfel. Improving solar cell efficiencies by down-conversion of high-energy photons. *Journal of Applied Physics*, 92(3):1668–1674, 2002.

21. B.S. Richards. Luminescent layers for enhanced silicon solar cell performance: Down-conversion. *Solar Energy Materials and Solar Cells*, 90(9):1189 – 1207, 2006.

22. Millicent B. Smith and Josef Michl. Singlet fission. *Chemical Reviews*, 110(11):6891–6936, 2010. PMID: 21053979.

23. Daniel N. Congreve, Jiye Lee, Nicholas J. Thompson, Eric Hontz, Shane R. Yost, Philip D. Reusswig, Matthias E. Bahlke, Sebastian Reineke, Troy Van Voorhis, and Marc A. Baldo. External quantum

efficiency above 100% in a singlet-exciton-fission–based organic photovoltaic cell. *Science*, 340(6130):334–337, 2013.

24. A. Rao and R. H. Friend. Harnessing singlet exciton fission to break the Shockley-Queisser limit. *Nature Reviews Materials*, 2:17063, November 2017.

25. Charles L. Braun. Electric field assisted dissociation of charge transfer states as a mechanism of photocarrier production. *The Journal of Chemical Physics*, 80(9):4157–4161, 1984.

26. Deibel Carsten, Strobel Thomas, and Dyakonov Vladimir. Role of the charge transfer state in organic donor acceptor solar cells. *Advanced Materials*, 22(37):4097–4111.

27. Koster L. Jan Anton, Shaheen Sean E., and Hummelen Jan C. Pathways to a new efficiency regime for organic solar cells. *Advanced Energy Materials*, 2(10):1246–1253.

28. D. L. Dexter. A theory of sensitized luminescence in solids. *The Journal of Chemical Physics*, 21(5):836–850, 1953.

29. T. Forster. Energiewanderung und Fluoreszenz. *Naturwissenschaften*, 33:166–175, June 1946.

30. Robert M Clegg. Fluorescence resonance energy transfer. *Current Opinion in Biotechnology*, 6(1):103 – 110, 1995.

31. T Ha, T Enderle, D F Ogletree, D S Chemla, P R Selvin, and S Weiss. Probing the interaction between two single molecules: fluorescence resonance energy transfer between a single donor and a single acceptor. *Proceedings of the National Academy of Sciences*, 93(13):6264–6268, 1996.

32. Stephen W. Clark, Jeffrey M. Harbold, and Frank W. Wise. Resonant energy transfer in pbs quantum dots. *The Journal of Physical Chemistry C*, 111(20):7302–7305, 2007.

33. Aaron R. Clapp, Igor L. Medintz, J. Matthew Mauro, Brent R. Fisher, Moungi G. Bawendi, and Hedi Mattoussi. Fluorescence resonance energy transfer between quantum dot donors and dye-labeled protein acceptors. *Journal of the American Chemical Society*, 126(1):301–310, 2004. PMID: 14709096.

34. Jonathan J. Burdett, Astrid M. Mueller, David Gosztola, and Christopher J. Bardeen. Excited state dynamics in solid and monomeric tetracene: The roles of superradiance and exciton fission. *The Journal of Chemical Physics*, 133(14):144506, 2010.

35. Oleksandr Voznyy, Larissa Levina, Fengjia Fan, Grant Walters, James Z. Fan, Amirreza Kiani, Alexander H. Ip, Susanna M. Thon,

Andrew H. Proppe, Mengxia Liu, and Edward H. Sargent. Origins of stokes shift in pbs nanocrystals. *Nano Letters*, 17(12):7191–7195, 2017. PMID: 29077419.

36. Nicholas J. Thompson, Mark W B Wilson, Daniel N Congreve, Patrick R. Brown, Jennifer M. Scherer, Thomas S. Bischof, Mengfei Wu, Nadav Geva, Matthew L. Welborn, Troy A. Van Voorhis, Vladimir Bulovic, Moungi G Bawendi, and Marc A. Baldo. Energy harvesting of non-emissive triplet excitons in tetracene by emissive pbs nanocrystals. *Nature materials*, 13 11:1039–43, 2014.

37. Nathaniel J. L. K. Davis, Jesse R. Allardice, James Xiao, Anthony J. Petty, Neil C. Greenham, John E. Anthony, and Akshay Rao. Singlet fission and triplet transfer to pbs quantum dots in tips-tetracene carboxylic acid ligands. *The Journal of Physical Chemistry Letters*, 9(6):1454–1460, 2018. PMID: 29506386.

38. A C Johnson, J R Petta, Jacob Taylor, Amir Yacoby, M D Lukin, Charles Marcus, Maxwell Hanson, and A C Gossard. Triplet-singlet spin relaxation via nuclei in a double quantum dot. 435:925–8, 07 2005.

39. A. P. Alivisatos. Semiconductor clusters, nanocrystals, and quantum dots. *Science*, 271(5251):933–937, 1996.

40. Iwan Moreels, Karel Lambert, Dries Smeets, David De Muynck, Tom Nollet, JosÃ© C. Martins, Frank Vanhaecke, AndrÃ© Vantomme, Christophe Delerue, Guy Allan, and Zeger Hens. Size-dependent optical properties of colloidal pbs quantum dots. *ACS Nano*, 3(10):3023–3030, 2009. PMID: 19780530.

41. Inuk Kang and Frank W. Wise. Electronic structure and optical properties of pbs and pbse quantum dots. *J. Opt. Soc. Am. B*, 14(7):1632–1646, Jul 1997.

42. L. Dal Negro, L. Pavesi, G. Pucker, G. Franzo, and F. Priolo. Optical gain in silicon nanocrystals. *Optical Materials*, 17(1):41 – 44, 2001. Optoelectronics I: Materials and Technologies for Optoelectronic Devices.

43. B. Wieb van der Meer, George Coker, and S.-Y. Simon Chen. *Resonance energy transfer : theory and data*. New York : VCH, 1994. Includes bibliographical references and index.

44. Aydan Yeltik, Burak Guzelturk, Pedro Ludwig Hernandez-Martinez, Alexander O. Govorov, and Hilmi Volkan Demir. Phonon-assisted exciton transfer into silicon using nanoemitters: The role of phonons and temperature effects in foerster resonance energy transfer. *ACS Nano*, 7(12):10492–10501, 2013. PMID: 24274734.

45. B M. Craig. Refractive indices of some saturated and monoethenoid fatty acids and methyl esters. 31:499–504, 02 2011.

46. Mercaptoacetic acid. https://www.chemicalbook.com/ProductMSDSDetailCB6477604_EN.htm. Accessed: 2018-07-16.

47. Iwan Moreels, Yolanda Justo, Bram De Geyter, Katrien Haustraete, JosÃ© C. Martins, and Zeger Hens. Size-tunable, bright, and stable pbs quantum dots: A surface chemistry study. *ACS Nano*, 5(3):2004–2012, 2011. PMID: 21355621.

48. Octavi E. Semonin, Justin C. Johnson, Joseph M. Luther, Aaron G. Midgett, Arthur J. Nozik, and Matthew C. Beard. Absolute photoluminescence quantum yields of ir-26 dye, pbs, and pbse quantum dots. *The Journal of Physical Chemistry Letters*, 1(16):2445–2450, 2010.

49. M. Greben, A. Fucikova, and J. Valenta. Photoluminescence quantum yield of pbs nanocrystals in colloidal suspensions. *Journal of Applied Physics*, 117(14):144306, 2015.

50. Gleb M. Akselrod, Mark C. Weidman, Ying Li, Christos Argyropoulos, William A. Tisdale, and Maiken H. Mikkelsen. Efficient nanosecond photoluminescence from infrared pbs quantum dots coupled to plasmonic nanoantennas. *ACS Photonics*, 3(10):1741–1746, 2016.

51. Aleksandr P. Litvin, Anton A. Babaev, Peter S. Parfenov, Elena V. Ushakova, Mikhail A. Baranov, Olga V. Andreeva, Kevin Berwick, Anatoly V. Fedorov, and Alexander V. Baranov. Photoluminescence of lead sulfide quantum dots of different sizes in a nanoporous silicate glass matrix. *The Journal of Physical Chemistry C*, 121(15):8645–8652, 2017.

52. Gleb Akselrod, Parag B Deotare, Nicholas J Thompson, Jiye Lee, William Tisdale, Marc A Baldo, Vinod Menon, and Vladimir Bulovic. Visualization of exciton transport in ordered and disordered molecular solids. 5:3646, 04 2014.

53. Vaubel G. and Kallmann H. Diffusion length and lifetime of triplet excitons and crystal absorption coefficient in tetracene determined from photocurrent measurements. *physica status solidi (b)*, 35(2):789–792.

54. American society for testing and materials (astm) terrestrial reference spectra for photovoltaic performance evaluation: Reference solar spectral irradiance: Air mass 1.5. https://rredc.nrel.gov/solar/spectra/am1.5/#about. Accessed: 2018-07-16.

55. Zeger Hens and Iwan Moreels. Light absorption by colloidal semiconductor quantum dots. *J. Mater. Chem.*, 22:10406–10415, 2012.

56. P. Wolber. An analytic solution to the Förster energy transfer problem in two dimensions. *Biophysical Journal*, 28:197–210, November 1979.

57. Green Martin A. and Keevers Mark J. Optical properties of intrinsic silicon at 300 k. *Progress in Photovoltaics: Research and Applications*, 3(3):189–192.

58. M. Morita, T. Ohmi, E. Hasegawa, M. Kawakami, and M. Ohwada. Growth of native oxide on a silicon surface. *Journal of Applied Physics*, 68(3):1272–1281, 1990.

59. Hines M.A. and Scholes G.D. Colloidal pbs nanocrystals with size-tunable near-infrared emission: Observation of post-synthesis self-narrowing of the particle size distribution. *Advanced Materials*, 15(21):1844–1849.

60. Ruirt Bosma. Size-dependent open-circuit voltage in lead sulfide colloidal quantum dot solar cells.

61. Lan Xinzheng, Voznyy Oleksandr, Kiani Amirreza, GarcÃa de Arquer F. Pelayo, Abbas Abdullah Saud, Kim Gi-Hwan, Liu Mengxia, Yang Zhenyu, Walters Grant, Xu Jixian, Yuan Mingjian, Ning Zhijun, Fan Fengjia, Kanjanaboos Pongsakorn, Kramer Illan, Zhitomirsky David, Lee Philip, Perelgut Alexander, Hoogland Sjoerd, and Sargent Edward H. Passivation using molecular halides increases quantum dot solar cell performance. *Advanced Materials*, 28(2):299–304.

62. Rachelle Ihly, Jason Tolentino, Yao Liu, Markelle Gibbs, and Matt Law. The photothermal stability of pbs quantum dot solids. *ACS Nano*, 5(10):8175–8186, 2011. PMID: 21888407.

63. J-J. Ganem, S. Rigo, I. Trimaille, and G-N. Lu. Nra characterization of pretreatment operations of silicon. *Nuclear Instruments and Methods in Physics Research Section B: Beam Interactions with Materials and Atoms*, 64(1):784 – 788, 1992.

64. M. Morita, T. Ohmi, E. Hasegawa, M. Kawakami, and M. Ohwada. Growth of native oxide on a silicon surface. *Journal of Applied Physics*, 68(3):1272–1281, aug 1990.

65. Z. H. Lu, J. P. McCaffrey, B. Brar, G. D. Wilk, R. M. Wallace, L. C. Feldman, and S. P. Tay. Sio2 film thickness metrology by x-ray photoelectron spectroscopy. *Applied Physics Letters*, 71(19):2764–2766, 1997.

66. Z. H. Lu, J. P. McCaffrey, B. Brar, G. D. Wilk, R. M. Wallace, L. C. Feldman, and S. P. Tay. SiO[sub 2] film thickness metrology by x-ray photoelectron spectroscopy. *Applied Physics Letters*, 71(19):2764, nov 1997.

67. thermo scientific xps: Carbon. https://xpssimplified.com/elements/carbon.php. Accessed: 2018-07-16.

68. thermo scientific xps: Silicon. https://xpssimplified.com/elements/silicon.php. Accessed: 2018-07-16.

69. Justin R. Caram, Sophie N. Bertram, Hendrik Utzat, Whitney R. Hess, Jessica A. Carr, Thomas S. Bischof, Andrew P. Beyler, Mark W. B. Wilson, and Moungi G. Bawendi. Pbs nanocrystal emission is governed by multiple emissive states. *Nano Letters*, 16(10):6070–6077, 2016. PMID: 27627129.

70. Time correlated single photon counting. https://www.picoquant.com/images/uploads/page/files/7253/technote_tcspc.pdf. Accessed: 2018-07-16.

71. Van der waals radius of the elements. http://periodictable.com/Properties/A/VanDerWaalsRadius.v.html. Accessed: 2018-07-16.

Colophon

This document was typeset using the typographical look-and-feel `classicthesis` developed by André Miede. The style was inspired by Robert Bringhurst's seminal book on typography "*The Elements of Typographic Style*". `classicthesis` is available for both LaTeX and LyX:

http://code.google.com/p/classicthesis/

Final Version as of July 16, 2018 (`classicthesis` version 0.02).